Measurement of charge-changing cross section of neutron-rich nitrogen isotopes for determining their proton radii

By

Aritra Roy

A Thesis Submitted to
Saint Mary's University, Halifax, Nova Scotia
in Partial Fulfillment of the Requirements for
the Degree of Master of Science in Applied Science.

April 2024, Halifax, Nova Scotia

Approved: _____
Prof. Rituparna Kanungo
Supervisor

Approved: _____
Prof. Greg Christian
Committee Member

Approved: _____
Prof. Luigi Gallo
Committee Member

Approved: _____
Prof. David Hornidge
External Examiner

Date: April 11, 2024

Contents

List of Figures

List of Tables

Abstract

Measurement of charge-changing cross section of neutron-rich nitrogen isotopes for determining their proton radii

By Aritra Roy

Exploring neutron-rich nuclei near the drip-line exposes exotic phenomena, including neutron halo or skin and the (dis)appearance of the existing magic numbers. A systematic study of point proton radii along an isotopic chain provides insights into the extended neutron wavefunction's impact on protons. This work, conducted at RIKEN, Japan, presents the first determination of the charge-changing cross section (σ_{cc}) for ^{23}N as well as the σ_{cc} for ^{21}N, with a secondary beam energy of around 250A MeV. The measured σ_{cc} values for ^{21}N and ^{23}N were 752 ± 4 mb and 747 ± 3 mb, respectively. Their comparable σ_{cc} suggests that the center-of-mass of the two valence neutrons in ^{23}N is not spatially separated from that of the core. Combined with the previously reported σ_{cc} of ^{22}N, these results indicate a shell closure at N = 16 for nitrogen isotopes. A higher two-neutron separation energy in ^{23}N supports the presence of a shell closure at $N = 16$ and raises questions about the reported large matter radius of this drip-line nitrogen isotope.

April 11, 2024

Acknowledgements

I wish to express my profound gratitude to all those who played a significant role in this journey. Your steadfast support and encouragement have been invaluable, and I deeply appreciate your contributions.

First and foremost, I extend my deepest thanks to my supervisor, *Professor Rituparna Kanungo*. Her guidance and unswerving belief in my research have been pivotal in shaping the direction of this thesis. I am genuinely thankful for the numerous hours of discussions, both in-person and online, that have enriched my understanding of nuclear physics and life in general.

I also wish to sincerely thank my committee members, *Prof. Greg Christian* and *Prof. Luigi Gallo*, for their valuable advice and support throughout my research. Additionally, I want to recognize the collaborators at the RIKEN Nishina Center, Japan, and convey my appreciation to *Dr. Yoshiki Tanaka* and *Dr. Soumya Bagchi* for their insightful contributions during our research group meetings. My gratitude extends to all my former professors and teachers, particularly *Prof. Narayan Banerjee, Prof. Shantanu Basu*, and others, as well as those who supported me in various ways throughout my academic journey. Special appreciation goes to *Divyang* for the vibrant discussions we had, spanning physics and extending beyond the academic sphere.

Moving to a foreign country, far from my family, would have presented significant challenges. Despite the physical distance, I am grateful to my friends — *Arghya, Palta, Anoojit, Rick, Rishav, and Tanmay* — for having my back through countless online chats over the past years. I am also thankful to friends here in Canada — *David, Mukhwinder, Nikhil, Saurabh, and Gurmukh* — for making this place feel like home.

Lastly, I owe an immense debt of gratitude to my family. To my parents, sister, *Anish*, and my entire family, your love, encouragement, and faith in my abilities have been a constant source of strength and motivation throughout this journey. This thesis is the culmination of the collective support and encouragement I have received, and for that, I am genuinely grateful.

Chapter 1

Introduction

All visible matter is fundamentally composed of protons, neutrons, and electrons, with the attractive Coulomb force between positively charged protons and negatively charged electrons being responsible for holding atoms together. However, the mystery surrounding the nucleus persists, primarily due to the electromagnetic repulsion among its many protons. Despite being significantly heavier than electrons, protons and neutrons are confined to an extraordinarily minute space of 10^{-15} m, making them beyond the resolution of any microscope.

E. Rutherford, H. Geiger, and Marsden's famous gold foil experiment gave the first insight into a nucleus [1,2]. In 1914, while studying the scattering of α particles from a thin gold foil, E. Rutherford found that a fraction of α particles deflected at surprisingly large angles [2]. The results led to the planetary model of an atom where the electrons revolve around the protons. The discrepancy between atomic number (number of protons) and atomic mass hinted at the presence of a third neutral particle. Almost two decades later, in 1932, J. Chadwick completed the picture of an atom by adding a charge-less particle, the neutron, inside the nucleus [3]. However, the pinching question remained: why do protons not fly apart? The answer came two years later. In 1934, H. Yukawa proposed the particle exchange mechanism between nucleons (collective term for neutrons

and protons) which results in an attractive force [4]. The discovery of the lightest meson particle, pion, confirmed this mechanism [5]. The resultant attractive force later turned out to be the strongest among the four fundamental forces and is hence referred to as the *Strong Force*. Constant wrestling between repulsive electromagnetic and attractive strong force binds the nucleons. Only certain combinations of protons and neutrons can create a perfect balance between these two strongest forces of nature. As of now, about 300 nuclei have achieved this rare stability criterion and most of our understanding of nuclear models was formulated based largely on data from these stable nuclei. In principle, one can add neutrons or protons to a nucleus until the nuclear drip-line is reached, where the binding energy is not enough to prevent the last nucleon from "dripping" off the nucleus. The proton and neutron drip-lines form the boundaries of nuclear existence (Fig. 1.1).

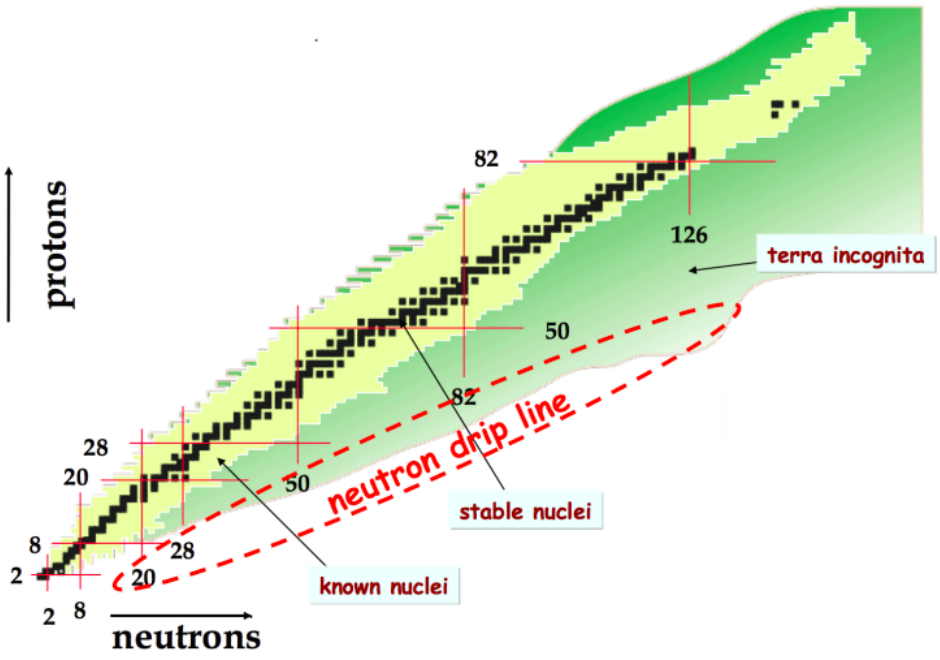

Figure 1.1: The nuclear landscape where each square represents a nucleus. The valley of stability is shown by black, unstable nuclei are represented by yellow and green region shows theoretically predicted bound nuclei. The magic numbers for the proton number (Z) and neutron number (N) are marked with horizontal and vertical red lines, respectively. Adapted from [6].

Although on the nuclear chart stable nuclei are confined to a narrow region called the valley of stability, unstable nuclei dominate the nuclear landscape. Despite a huge difference in their sizes, observations revealed striking similarities between the atom and the nucleus. A careful analysis of proton and neutron separation energies indicated the presence of a shell structure inside the nucleus [7]. The shell gaps, i.e. shell closures were observed at neutron and proton numbers of 8, 20, 28, 50, 82, and 126 which are referred to as the "magic numbers". The sudden decrease in the neutron-capture cross sections and the nuclear charge radius at magic numbers [8] strengthened the idea of shell existence. All evidence suggested the potential application of the atomic shell model concepts to the nucleus by assuming different spherically symmetric mean potentials, e.g., infinite square well, harmonic oscillator, and Woods-Saxon potential (WS). However, the energy levels predicted by considering a harmonic oscillator (HO) potential do not correspond to the empirical magic numbers except for the lowest few. In 1949, M. Mayer [8, 9] and O. Haxel et al. [10] (independently) successfully explained the magic numbers by incorporating the spin-orbit term in a nuclear potential.

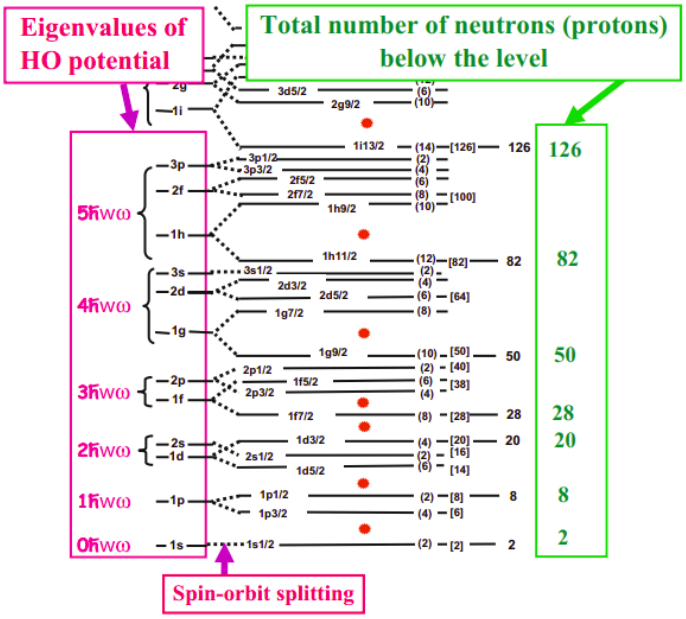

Figure 1.2: Mayer-Jensen's shell model scheme predicted with harmonic oscillator potential and the spin-orbit force. Figure adapted from [11].

Fig. 1.2 depicts the energy levels of harmonic oscillator potential and their splitting due to the spin-orbit coupling. Each energy level can accommodate 2j + 1 nucleons, where j is the total angular momentum. Unfortunately, aside from the lowest ones, these shells do not align with the observed magic numbers empirically. The shell model reproduces measured excitation energies, spin/parities for ground states and low-energy excited states. However, for some nuclei, the shell model could not predict magnetic dipole moments, electric quadruple moments, or excited state spectra. As a result, various models to account for the collective motion of nucleons were proposed.

In the mid-1980s, the availability of Rare Isotope Beams (RIBs) made possible the study of nuclei with extremely high ratios of neutrons (N) to protons (Z) [12, 13]. Such nuclei with $N/Z >> 1$ (or $Z/N >> 1$) ratios are referred to as exotic nuclei because they are exhibiting properties that don't align with the known model. On the nuclear chart, exotic nuclei can be found far away from the valley of stability, hence they are short-lived (few tens of milliseconds). This new arena is changing the conventional magic number paradigm. Interestingly, near the drip-line, where nucleon(s) is (are) at the brink of dripping from the core nucleus, some traditional magic numbers vanished and new ones appear instead (N= 16, 32) [14]. The following section provides an in-depth exploration of the observed properties exhibited by these highly asymmetric ($N/Z >> 1$) exotic nuclei in close proximity to the dripline.

1.1 Properties of exotic nuclei

Exploring the diverse properties of exotic nuclei is a prominent area of research in nuclear science, shedding light on the nature of the short-range nuclear forces and contributing to the understanding of the origin of chemical elements in the universe [15]. As discussed above, for exotic nuclei, the ratio of protons and neutrons is highly asymmetric. In the region near the drip-line (Fig. 1.1), the valence nucleons (usually neutrons)

are very weakly bound, giving rise to exotic properties like the formation of a halo and skin. Due to the absence of a confining Coulomb barrier, these features are prominent in neutron-rich nuclei compared to proton-rich nuclei.

1.1.1 Neutron skin

In stable nuclei, the one neutron separation energy(S_n) and one proton separation energy(S_p) are nearly equal. In addition, for light stable nuclei, the root mean square (r.m.s) radius of the proton distribution ($\langle r_p^2 \rangle^{\frac{1}{2}}$) is almost identical to the neutron distribution ($\langle r_n^2 \rangle^{\frac{1}{2}}$).

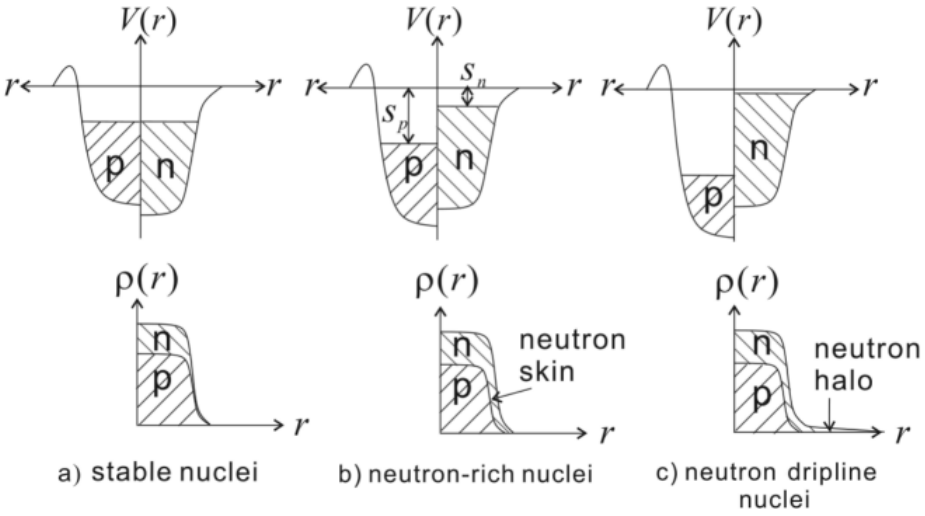

Figure 1.3: The mean field potential (top) and the density profile (bottom) for protons and neutrons. For (a) stable nuclei, $S_n = S_p$ and $\langle r_p^2 \rangle^{\frac{1}{2}} \approx \langle r_n^2 \rangle^{\frac{1}{2}}$ (b) neutron-rich nuclei, a significant difference in S_n and S_p results in a thick neutron skin; and (c) neutron drip-line nuclei, the valence neutron(s) forms a halo structure as $S_n = 0$. Figure adapted from [16].

However, for nuclei with a high N/Z ratio, the difference between S_n and S_p change drastically, as shown in 1.3(b). The neutron density extends significantly further than the proton density, forming a thick neutron skin. Neutron skin thickness (ΔR) is defined as a difference between the rms neutron and proton radius [17]:

$$\Delta R = R_n - R_p \tag{1.1}$$

The root mean square matter radius (R_m) is related to the root mean square neutron radius (R_n) and the root mean square proton radius (R_p) through the following equation:

$$R_m^2 = \frac{N}{A} \cdot R_n^2 + \frac{Z}{A} \cdot R_p^2 \tag{1.2}$$

Here, the atomic number is denoted as Z, the mass number as A, and the neutron number as N. The root mean square matter radius (R_m) incorporates the contributions of both neutron and proton distributions within the nucleus. The determination of R_n and ΔR can be achieved through measurements of the matter radius and proton radius, respectively, utilizing the Eq. 1.1 & 1.2.

1.1.2 Neutron halo

In nuclear physics, the term 'halo' refers to an extended surface of low density formed by one or two weakly bound neutrons around a core with similar density distributions for protons and neutrons. In some cases, introducing two neutrons to the core results in the formation of a three-body bound system, often referred to as a Borromean nucleus (e.g., ^{6}He, ^{11}Li, ^{22}C, etc.). This concept draws a parallel to Borromean rings, where each of the three rings is interlinked, and yet, there is no direct link between any two rings. For instance, the two-neutron halo nucleus, like ^{6}He, can be imagined as a three-body system composed of an alpha particle and two neutrons. It is interesting to note that ^{6}He is bound in this configuration, while neither ^{5}He nor the *dineutron* are bound.

Nuclear halos result from the spatial distribution of outermost neutrons, causing a low-density extended neutron surface and a notable increase in matter radius. A systematic study of the point proton radii (i.e. protons as point particle in the nucleus) along an isotopic chain reveals insights into the impact of the extended neutron wavefunction on protons. Halo occurrences in light neutron-rich nuclei such as ^{11}Li have led to a new era in nuclear science. These particular phenomena of exotic nuclei are of quantum me-

chanical origin and are well explained by considering the probability distribution of the least bound nucleon. For simplicity, if we assume the interaction potential is a square well between the halo neutron and the core, then under this scenario, the wave function of an s-wave neutron can be described as,

$$\psi(r) = \left(\frac{2\pi}{k}\right)\left(\frac{-e^{kr}}{r}\right)\left[\frac{e^{kR}}{(1+kR)^{1/2}}\right] \tag{1.3}$$

where, k is the slope of the density tail and R is the width of the potential [18]. Using this wavefunction, the asymptotic density tail ($\rho(r)$) of an s-wave neutron will be,

$$\rho(r) = \mid \psi(r) \mid^2 = \left(\frac{2\pi}{k}\right)^2\left(\frac{-e^{2kr}}{r^2}\right)\left[\frac{e^{2kR}}{(1+kR)}\right] \tag{1.4}$$

The parameter k in the given equations is intricately linked to the neutron separation energy (E_s), with its relationship expressed as $(\hbar k)^2 = 2\mu E_s$, where μ denotes the reduced mass of the system [17]. A diminished value of S_n contributes to a decrease in the parameter k, resulting in an elongated distribution tail in halo nuclei. In addition to a low separation energy, the presence of a small orbital angular momentum is a crucial prerequisite for a nucleus to exhibit a halo state. The higher angular momentum introduces an extra centrifugal barrier, reducing the likelihood of tunneling to a larger radius. Consequently, halos are anticipated to be more prevalent when valence neutrons occupy the s or p states [19]. The charge radius of a nucleus also serves as a significant parameter for identifying halo formation in neutron-rich nuclei. An isotopic charge radii chain can unveil signatures of shell closures as local minima [20]. Combining the knowledge of proton radii together with matter radii (distribution of nucleons in nuclei) enhances our understanding of these exotic nuclei and facilitates the derivation of their properties.

1.1.3 Change in magic numbers

Another interesting feature for exotic nuclei is the disappearance of conventional magic numbers such as $N = 8$ and 20, and the emergence of new magic numbers like N= 14 and 16. These features suggest a significant modification in the nuclear shell structure for nuclei in the neutron-rich region. The neutron number (N) dependence of experimentally observed neutron separation energies (S_n) reveals an anomaly in $p - sd$ and sd shell nuclei, as illustrated in Fig. 1.4. The separation energies of nuclei with the same isospin $T_z = (N - Z)/2$ are connected by lines, where the kinks represent the magic numbers. Notably, kinks are evident for magic numbers $N = 8$ and 20 in small T_z nuclei but disappear in large T_z nuclei. The absence of nucleon shell closure at $N = 8$ (kink) signifies disappearance of the shell gap for $p - sd$ shell nuclei. Additionally, a new magic

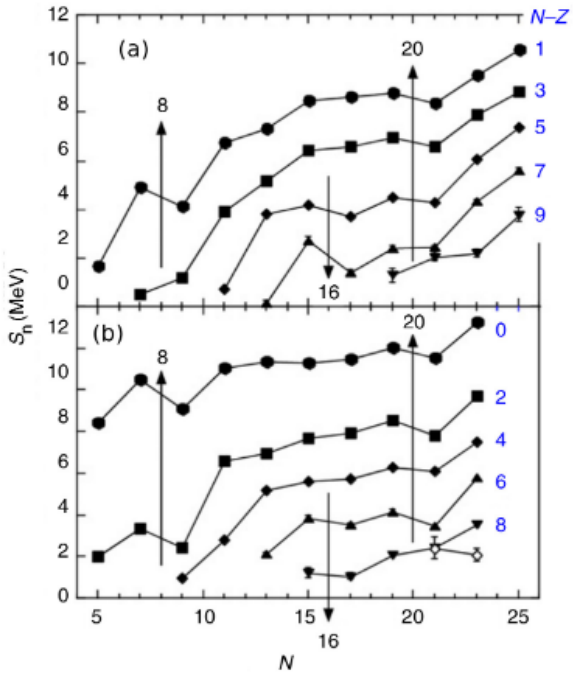

Figure 1.4: The dependence of neutron number (N) with the experimentally observed neutron separation energies (S_n) for nuclei with (a) odd N and even Z, and (b) odd N and odd Z. Numbers next to the line indicate $2T_z$. Figure adapted from [21].

number at $N = 16$ is suggested by the appearance of a kink for large isospin $T_z \geq 5/2$.

The tensor monopole interaction between proton and neutron orbit pairs with $j = l + \frac{1}{2}$ and $j = l - \frac{1}{2}$ is attractive in nature compared to pairs with $j = l + \frac{1}{2}$ and $j = l + \frac{1}{2}$ (or $j = l - \frac{1}{2}$ and $j = l - \frac{1}{2}$) [22]. Therefore, the valence neutron and valence proton orbits, along with the nature of their interaction (attraction/repulsion), determine the shell gaps between neighboring orbits and consequently influence shell closure. The proton radius (R_p) of $^{22}_{8}$O decreases along the oxygen isotopic chain and then increases again for ^{23}O, indicating the presence of a neutron sub-shell closure at $N = 14$ [23]. The origin of this $N = 14$ sub-shell closure is believed to stem from the attractive monopole proton-neutron interaction between the $p(1p_{1/2})$ and $n(1d_{5/2})$, leading to the lowering of the $n(1d_{5/2})$ orbital and the creation of an energy gap at $N = 14$.

1.2 Motivation to study neutron-rich nitrogen isotopes

Understanding the origins of the changes in shell structure is crucial to identifying the emerging signs of these changes. The presence of neutron halos in ^{11}Li and ^{11}Be relates to the breakdown of the N = 8 shell gap [24]. Evidence has been found for a new shell gap at N = 16 at the drip-line of carbon to fluorine isotopes. Studies of excited states and momentum distributions have discussed a shell gap at N= 14 between the $1d_{5/2}$ and $2s_{1/2}$ orbitals in oxygen isotopes. However, its reduction for the nitrogen isotopes is signalled and its disappearance due to level inversion of the $\nu 1s_{1/2}$ and the $\nu 0d_{5/2}$ levels is predicted in the carbon isotopes [25–29]. A reduction in the width of the longitudinal momentum distributions ($\Delta P_{||}$) between ^{21}N ($\Delta P_{||} = 160 \pm 32$ MeV/C) and ^{22}N ($\Delta P_{||} = 77 \pm 32$ MeV/C) from one neutron removal reaction indicate a change of dominating neutron orbitals from l = 2 to l = 0 in ^{21}N and ^{22}N, respectively [25]. The $P_{||}$ for ^{18,19}N are explained by $\sim$ 69% probability of the neutron in the l = 2 orbital with the core nucleus in excited states. The situation changes in ^{20,21}N where the $P_{||}$ are explained with 83% and 68% probability, respectively of valence neutrons in the

$l = 2$ orbital with the core in its ground state. A shell gap at $N = 14$ in ^{22}O was first indicated from the high excitation energy of its first excited state [30]. Proton inelastic scattering [31] affirms this, implying a small quadrupole deformation ($\beta = 0.26(4)$) and an electric quadrupole transition probability [$B(E2)$] value deduced to be 21(8) e^2fm^4. However, proton inelastic scattering of ^{21}N is consistent with a much larger $B(E_2)$ value of 56(18) e^2fm^4 [27], and it indicates a reduction of the $N = 14$ shell gap by 1.2 MeV when transitioning from O to N. Recently, quasifree knockout reaction studies of ^{22,23}O and ^{21}N show a decrease in the width of the momentum distribution in going from ^{22}O to ^{21}N suggesting a reduced N= 14 shell gap for this nucleus leading to more configuration mixing of the $2s_{1/2}$ orbital [32]. This shell gap was found to be strongly reduced to 1.41(17) MeV in ^{22}N and predicted to disappear in the carbon isotopes [26]. Ref. [33] however deduces a moderately large energy gap of 3.02 MeV at N = 14 from the excited states in ^{21}N.

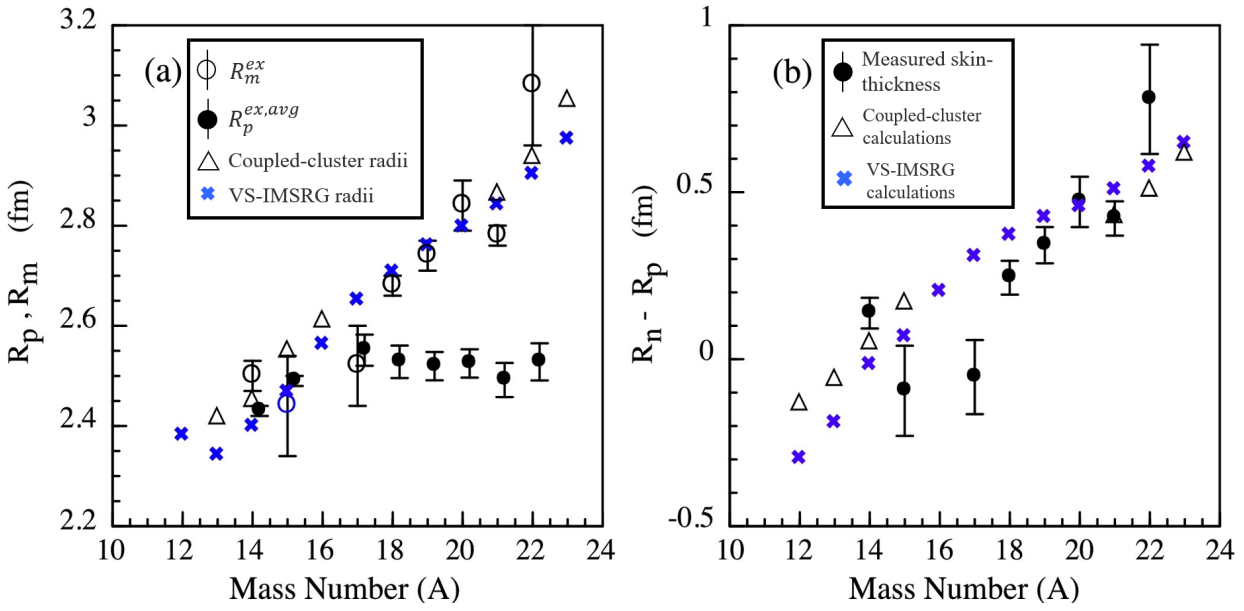

Figure 1.5: The experimental point matter radii (black open circles) and (b) measured neutron skin thicknesses (black filled circles) are compared to the respective theoretical calculations. The experimental point proton radii, $R_p^{ex,avg}$, are shown by black-filled circles in (a) where those for ^{14,15}N are from e^- scattering. The blue crosses correspond to VS-IMSRG radii, the black open triangles are coupled-cluster radii computed with oxygen cores. Figure adapted from [34].

In 2019, S. Bagchi et al. [34] reported the point proton radii of $^{17-22}$N measured from charge-changing cross sections (σ_{cc}) on a carbon target at $\sim 900A$ MeV. A thick neutron skin for $^{19-21}$N is reported, while for ^{22}N a neutron halo-like structure develops. The rapid increase in the nuclear matter radii, as observed from ^{22}N (3.07 ± 0.13 fm)(Fig. 1.5) to ^{23}N (3.41 ± 0.23 fm) [35], hints towards the halo structure of ^{23}N. A decrease (within uncertainties) in the point-proton radii from ^{17}N to ^{21}N is also reported [34], which may reflect a transition from deformation towards sphericity at the N = 14 shell closure. The notable increase in radius beyond ^{21}N may be attributed to the influence of the $2s_{1/2}$ neutron in ^{22}N. The sudden increase in the proton radius beyond ^{21}N highlights the critical necessity of investigating the proton radius of ^{23}N for a comprehensive understanding of the nitrogen isotope chain. Given the absence of available data on the proton radius of this drip line nucleus with N=16, this study aims to make the first determination of the point proton radius for ^{23}N. The derived proton radius from this investigation, along with the previously reported significantly large matter radius of ^{23}N, provides valuable insights into the structural features of this neutron-rich isotope. The halo formation due to the large matter radius of ^{23}N is challenged by the stronger binding of the valence neutrons. The two-neutron separation energy (S_{2n}) of ^{23}N is 4.7 MeV, higher than both its single-neutron separation energy (3.12 MeV) and single-neutron separation energy (S_n) of ^{22}N (1.28 MeV) [36,37] obtained using Eq. 1.5. Hence, the obtained proton radius from this study will be extremely useful to further constrain the structure of this dripline nitrogen isotope. Consequently, the findings of this study promise to shed light on the presence of the N = 16 magic number in the nitrogen isotopic chain.

$$\begin{aligned} S_n &= -M(A,Z) + M(A-1,Z) + n \\ S_{2n} &= -M(A,Z) + M(A-2,Z) + 2n \end{aligned} \tag{1.5}$$

Therefore, a systematic study of the point proton radii along the nitrogen isotopic chain is necessary to evaluate the impact of the extended neutron wavefunction on pro-

tons. Systematic trends of proton radii along the nitrogen isotopic chain can reveal the presence of neutron magic numbers [38]. This study also includes the measurement of ^{21}N at a different beam energy than that reported in Ref. [34], which will serve as a comparison point to its radius derived from the previous study at GSI. This will allow an assessment of the need for scaling factor for the σ_{cc} as reported in earlier works in the intermediate energy-range.

1.3 Conventional methods to determine the proton distribution radii

The matter radii of unstable nuclei have been primarily derived by analyzing interaction cross sections [35,39]. However, data on proton radii for unstable nuclei is scarce. Below is a summary of various methods for measuring the proton distribution radii.

1.3.1 Electron scattering

Electron scattering provides the most accurate information about the charge distribution in nuclei and nucleon structure. This method avoids the complications of strong interactions between the projectile and target, making it a precise tool for studying the distribution of charges in nuclei. The focus is solely on elastic electron scattering when examining the charge distribution in nuclei. The differential cross section for elastic scattering from a spinless nucleus using the Plane-Wave Impulse-Approximation (PWIA) is expressed as [40],

$$\frac{d\sigma}{d\Omega} = \frac{d\sigma_{Mott}}{d\Omega} \mid F_c(q) \mid^2 \tag{1.6}$$

where $F_c(q)$ is the charge form factor and $d\sigma_{Mott}/d\Omega$ is the Mott cross section which is the elastic scattering cross section and for a point particle of charge Z, it is expressed

as,

$$\frac{d\sigma_{Mott}}{d\Omega} = \frac{(Z\alpha)^2 \cos^2(\frac{\theta}{2})}{4e^2 \sin^4(\frac{\theta}{2})} \tag{1.7}$$

here, θ is the scattering angle, e is the electron charge, and α is the fine-structure constant. The form factor is a Fourier transform of the charge distribution $(\rho_c(r))$, for momentum transfer, q,

$$F_c(q) = \frac{1}{2\pi^{3/2}} \int \rho_c(r) e^{-iq\cdot\vec{r}}\, r d\vec{r} \tag{1.8}$$

The charge distribution $(\rho_c(r))$ of a target nucleus can be determined through the inverse Fourier transformation of the charge form factor, which is experimentally obtained.

Elastic electron scattering measurements have been used to determine the charge radii or proton distribution radii of stable nuclei. The elastic electron scattering data for long-lived nuclei ^{3}He and ^{14}C have been analyzed [41, 42], but no studies of nuclei far from the stability line have been reported as of yet, as it requires long-half lives to prepare a sufficiently thick radioactive target. However, the Self-Confining RI Ion Target (SCRIT) electron scattering facility at the RIKEN RI beam factory in Japan aims to study the internal nuclear structure of these unstable nuclei through its innovative internal target system [43].

1.3.2 Muonic atom x-ray spectroscopy

Muons are used to study the charge distribution of nuclei by forming muonic atoms. Negative muons are fired at a target material which when captured, orbit the nucleus closely due to their greater mass. This results in a cascade of muonic transitions emitting X-rays and Auger electrons, and enables the determination of charge radii of most stable elements through Muonic X-ray spectroscopy [38, 44], due to the sensitivity of low-lying muonic transitions to nuclear charge distribution. However, this method is not suitable

for investigating radioactive nuclei as it requires several tens of milligrams of the target material. Efforts are underway to extract the nuclear charge radii of radioactive isotopes using only a few micrograms of the target [45].

1.3.3 Isotope shift

The charge distribution within a nucleus can be determined through isotope shifts for lighter elements. This has been the most commonly used method to determine the charge radii of nuclei far from stability among electron scattering, muonic atoms, and isotope shift. Isotope shift measurements consist of two components, the mass shift (MS) and the volume shift or field shift (FS), that reveal the charge radius information. The mass shift refers to the change in nuclear mass between two isotopes, while the volume shift reflects the difference in the charge distribution within a nucleus. The measurement of charge radii in lithium isotopes through isotope shift provided a model-independent value of the charge radius of the ^{11}Li nucleus, which is a Borromean halo nucleus [46,47]. In the case of light nuclei, the mass shift is the dominant factor and decreases quickly with increasing mass number as A^{-2}. In contrast, the volume shift or field shift is more pronounced in heavy elements, increasing with the nuclear charge number Z as $Z^2\,A^{-1/3}$. Determining the charge radius of light nuclei through isotope shift measurements is difficult and can only be done on very simple and stable atoms with no more than two electrons. To achieve this, an extremely accurate theoretical calculation of the atomic structure contributing to the MS of at least one reference isotope is necessary. The difference in charge radius is then obtained by comparing the experimentally observed isotope shift to the atomic theory calculations. This method was used to determine the ^{6}He nuclear charge radius using the charge radius of ^{4}He measured through electron scattering and muonic atom spectroscopy and the difference in charge radius from the ^{4}He $-^6$ He isotope shift measurement [48,49]. A similar approach was applied to determine the charge radii of Be [50] isotopes, as shown in Fig. 1.6. An interesting pattern is

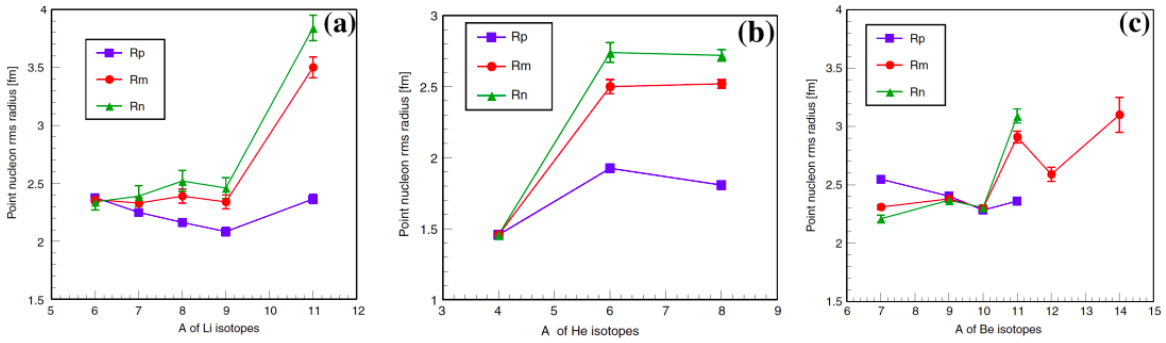

Figure 1.6: The radii of point nucleon distribution in (a) Li isotopes (b) He isotopes (c)Be isotopes. Figures adapted from [24].

seen in isotopic chains where the proton radius increases when a neutron halo is formed, such as in ^{11}Li, ^{6}He, and ^{11}Be. Surprisingly, there is a decrease in charge radius from ^{6}He to ^{8}He despite an increase in matter radius with a higher nucleon number. In Borromean halo ^{6}He, the correlated pair of neutrons moving against the recoil motion of the α-like core smears the charge distribution, resulting in an increase in charge radius. However, in ^{8}He, the recoil effect is believed to be smaller due to a possibly spherical distribution of the four extra neutrons around the α-like core, thus resulting in a less spread charge distribution and a smaller charge radius in comparison to ^{6}He. The isotope shift method was used to determine the charge radii of ^{41,51,52}Ca [51]. The unexpectedly large charge radius of ^{52}Ca compared to theoretical predictions has raised new questions on the change in nuclear structure in unstable neutron-rich nuclei. However, studying the light neutron-rich nuclei through isotope shift is challenging, as it requires the production of low-energy, high-intensity beams of short-lived isotopes, which is difficult. The atomic structure calculations also become complex due to many-body electron correlations in the atoms.

1.3.4 Charge-changing cross section measurement

Charge-changing cross section (σ_{cc}) measures the change in the atomic number of a projectile nucleus due to interaction with protons in the nucleus. This helps to determine the point-proton radius using the Glauber model theory. Webber et al. [52] and Cummings et al. [53] used σ_{cc} to study the interstellar production of cosmic-ray fragments and so to determine elemental and isotopic components of cosmic rays. Blank et al. [54] measured σ_{cc} of neutron-rich lithium isotopes to examine proton distribution. Chulkov et al. [55] measured σ_{cc} of light stable and neutron-rich nuclei (^{14}Be, $^{10-19}$B, $^{12-20}$C, $^{14-23}$N, $^{16-24}$O, and $^{18-27}$F), but the results were higher than previous studies and could not be explained by proton radii from electron scattering, suggesting a systematic uncertainty. The finite range Glauber model theory will be presented in the following section.

Finite range Glauber model

The measurement of σ_{cc} has the advantage of allowing the cross section of many nuclei to be measured using the same setup as for reaction/interaction cross section, which is crucial in determining the matter distribution within a nucleus. A theoretical tool based on the Glauber model framework [56] is widely used to calculate the reaction cross section of projectile-target collisions by integrating the reaction probability over the two-dimensional impact parameter vector b and is given by,

$$\sigma_R = \int [1 - T(\boldsymbol{b})]\, d\boldsymbol{b} \tag{1.9}$$

The transmission function, $T(b)$, is the likelihood of the projectile passing through the target without interaction, given the impact parameter b. Meanwhile, the charge-changing cross section (σ_{cc}) only involve the interaction of the protons of the projectile nucleus. Thus, σ_{cc} can be written as,

$$\sigma_{cc} = \int d\boldsymbol{b} P_{cc}(\boldsymbol{b}) \tag{1.10}$$

where $P_{cc}(b)$ is the probability of charge changing reaction at the impact parameter b. $P_{cc}(\mathbf{b})$ is calculated using Optical Limit Approximation (OLA) [56, 57]. The Glauber model assumes that at high energies, the nucleons have enough momentum while the nuclei pass each other, resulting in nearly undeflected scattering. The probability of charge changing reaction, $P_{cc}(b)$, is given by [58],

$$P_{cc}(\boldsymbol{b}) = 1 - \exp\left(-2\sum_{N=p,n}\int\int d\boldsymbol{s}\, d\boldsymbol{t}\, T_P^{(p)}(\boldsymbol{s})\, T_T^N(\boldsymbol{t}) \times \mathrm{Re}\,\Gamma_{pN}(\boldsymbol{b}+\boldsymbol{s}-\boldsymbol{t})\right) \tag{1.11}$$

where s is the two-dimensional vector of the projectile's single particle coordinate, r, measured from the projectile's c.m. coordinates, and t is defined for the target nucleus in a similar way. $T_P^{(p)}(s)$ is the thickness function of the projectile's proton density $\rho_P^p(r)$ [23],

$$T_P^{(p)}(\boldsymbol{s}) = \int_{-\infty}^{\infty} dz\, \rho_P^{(p)}(\boldsymbol{r})\ ;\boldsymbol{r} = (\boldsymbol{s}, z) \tag{1.12}$$

The finite-range profile function, $\Gamma_{NN}(\mathbf{b})$, for the nucleon-nucleon (NN) scattering is parameterized as [59]:

$$\Gamma_{NN}(\boldsymbol{b}) = \frac{1 - i\alpha_{NN}}{4\pi\beta_{NN}}\,\sigma_{NN}^{tot}\exp\left(-\frac{\boldsymbol{b}^2}{2\beta_{NN}}\right) \tag{1.13}$$

In equation 1.13, α_{NN} is the ratio of the real to the imaginary part of the NN scattering amplitude; β_{NN} is the finite range parameter i.e the slope parameter of the NN elastic differential cross section; and σ_{NN}^{tot} is the total cross section for NN collisions. The parameters for the NN profile functions are listed in [59] for various energies. By using these parameters of nucleon-nucleon cross sections and applying the Glauber model

framework to a target with a known density distribution, the point proton radii can be determined.

R_p determined from σ_{cc}

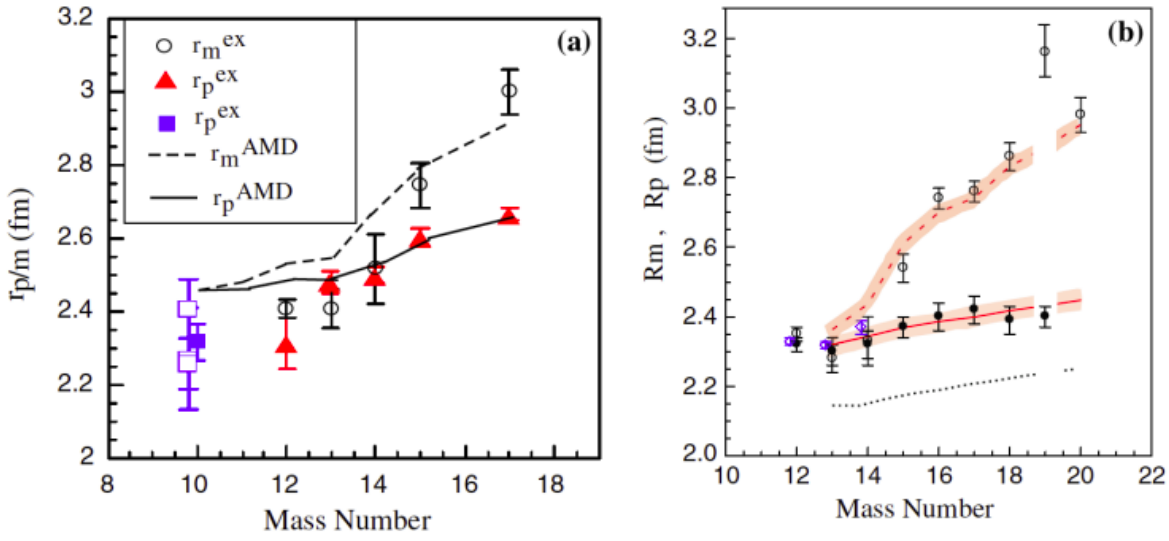

Figure 1.7: The measured R_m (circles) and measured R_{cc}^p (triangles) for $^{12-17}$B (b) The measured R_m (open circles) and measured R_{cc}^p (filled circles) for $^{12-19}$C. The blue symbols represent the measured R_p derived from e scattering. Figure adapted from [60, 61].

The proton radii determined from the charge-changing cross section (σ_{cc}) are referred to as R_{cc}^p in the following. Estrade et al. [60] used a finite-range Glauber model to determine the proton radii (R_{cc}^p) of $^{10-17}$B. The results (red triangles in Fig. 1.7 (a)) were consistent with electron scattering experiments (blue squares in Fig. 1.7 (a)), showing a thick neutron skin of 0.51 ± 0.11 fm in ^{17}B. Yamaguchi et al. [62] also used the zero range Glauber model to determine the proton radii of $^{9-10}$Be, $^{14-16}$C and $^{16-18}$O at 300A MeV, but had to introduce a universal scaling of the measured σ_{cc} ($\mathcal{F} = \sigma_{cc}^{expt}/\sigma_{cc}^{calc} = 1.05 \pm 0.03$) to reproduce the proton radii from electron scattering measurements. However no scaling was required in Ref. [60]. The Glauber model has also been successfully used to extract radii of $^{12-14}$C [61] and ^{14}N [34] at $800 - 900A$ MeV, consistent with electron scattering results. The proton radii of the carbon isotopic

chain show an evolution of thick neutron surface from 0.5 fm in ^{15}C to 1 fm in ^{19}C, as shown in Fig. 1.7 (b). The halo radius of ^{19}C was found to be 6.4 ± 0.7 fm, similar to ^{11}Li. The radii of $^{13-18}$C also agree with *ab initio* calculations that use chiral nucleon-nucleon and three-nucleon forces.

The upcoming chapters of this thesis are classified as follows:

- Chapter 2 provides details on the measurement principle, along with a description of the detectors used in this experiment, explaining their working principles.

- Chapter 3 presents the techniques employed for analyzing data obtained from different sets of detectors.

- Chapter 4 discusses and concludes the results obtained from the experiment, presenting the future outlook of this study.

Chapter 2

Experimental setup and methodology

The measurement of charge-changing cross-sections of neutron-rich nitrogen isotopes was carried out using BigRIPS fragment separator and Zero Degree Spectrometer (ZDS) at the RI Beam Factory (RIBF) [63] in Japan. RIBF, operated by RIKEN Nishina Center, features a high-power heavy-ion accelerator with three ring cyclotrons (fixed-frequency (fRC), intermediate-stage (IRC) and superconducting cyclotron (SRC)), capable of boosting light ion beams up to 440A MeV and heavy ion beams up to 350A MeV.

2.1 Radioactive Ion beam production at RIBF

The Radioactive Isotope Beam Factory is an advanced facility aiding researchers in understanding the formation of heavy elements in the universe. Recent upgrades enable the RIBF to produce intense beams of approximately 4,000 unstable nuclei, extending our exploration beyond the limit of known nuclei [65]. As an in-flight facility, RIBF generates secondary beams through projectile fragmentation, necessitating a primary beam, target, mass separator, spectrometer, and beam transport system. At RIBF, the radioactive isotope (RI) beams of ^{21,23}N are produced by high-energy primary beam of ^{48}Ca accelerated to 345A MeV to interact with a 10 mm thick rotating ^{9}Be target. Fig. 2.1 illustrates a schematic view of the RI Beam Factory at RIKEN Nishina Center.

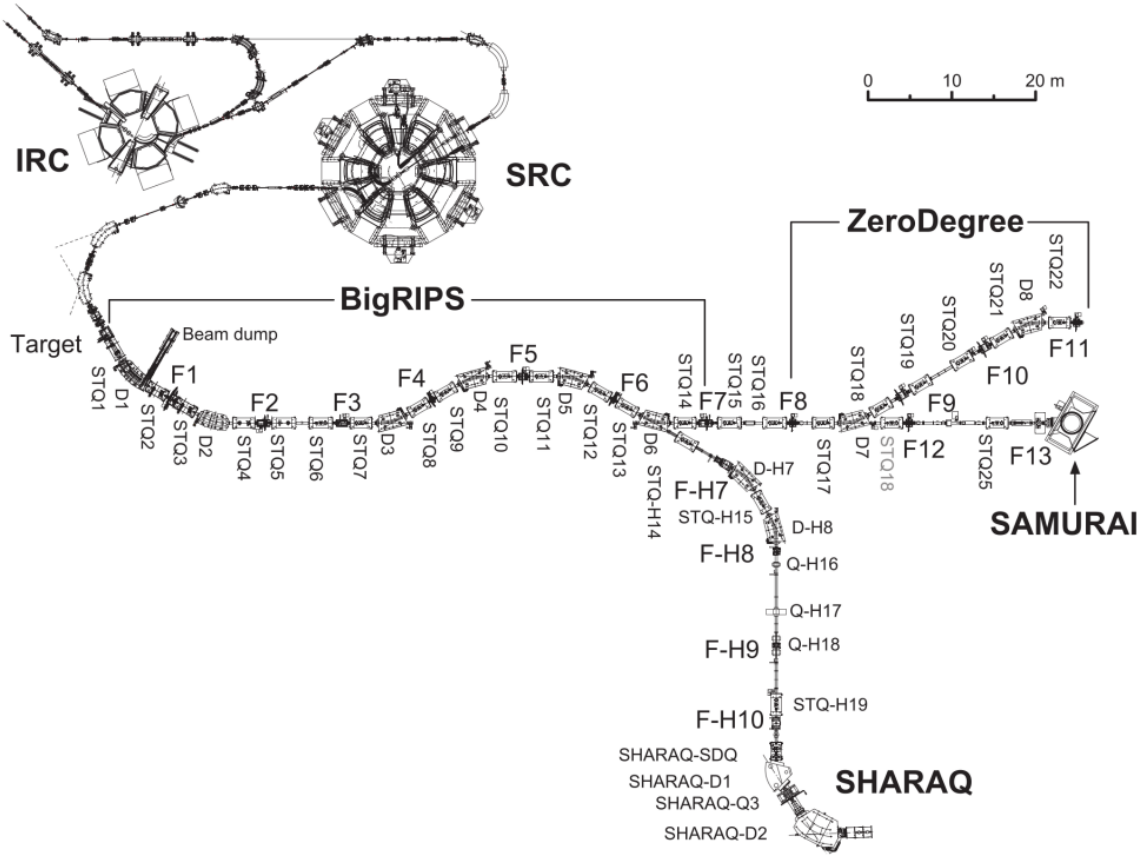

Figure 2.1: The schematic view of RIBF at RIKEN Nishina Center [64].

2.2 Fragment Separator at BigRIPS

The BigRIPS separator is a 78.2m long, two-stage high-resolution spectrometer that selectively delivers isotopic fragments. It has large-ion optical acceptances and particle identification capabilities. The first stage operates in separator mode, as depicted in Fig. 2.2, and uses an energy degrader to separate the desired nuclei from the projectile fragments. The second stage of the BigRIPS is a spectrometer designed to identify the fragments produced in the first stage for further secondary reaction analysis.

The first stage of BigRIPS includes two 30^{o} room-temperature dipole magnets (RTDs) and a set of large-aperture superconducting quadrupoles (STQs) with large acceptances. Its design enhances the accessible region of secondary reactions, increasing fragment col-

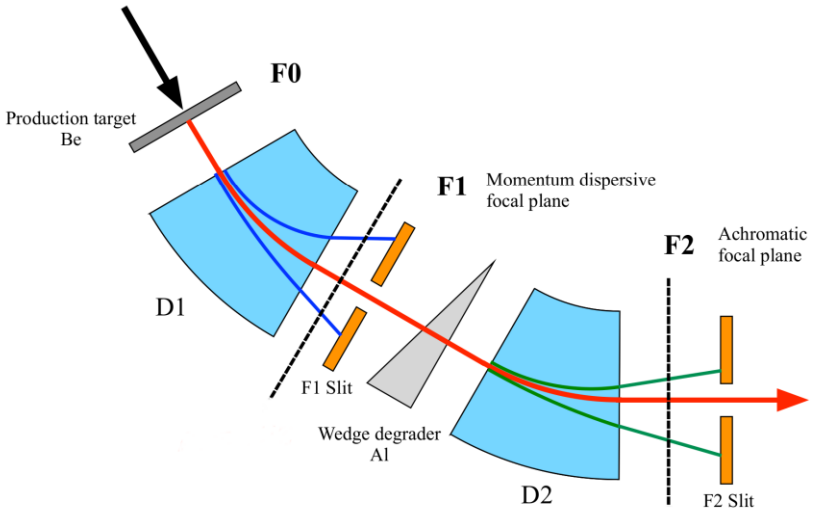

Figure 2.2: Schematic drawing of the separation of RI beams in the 1^{st} stage of BigRIPS [66].

lection efficiency. BigRIPS is a two-bend achromat system with a momentum-dispersive focus at F1 and an achromatic focus at F2. The separated fragments are transported from the first stage to the second stage as shown in Fig. 2.2.

The second stage of BigRIPS consists of four dipole magnets and eight superconducting quadrupoles, forming a 4-bend achromat system. The system spans from the experimental focus F3 to F7, with F3 and F7 being achromatic and the intermediate focal planes F4, F5, and F6 being momentum-dispersive. The stage uses time-of-flight (TOF), energy loss (ΔE), and magnetic rigidity (χ) to identify isotopes produced in secondary reactions, based on event-by-event information. After the BigRIPS separator, the beam transport system operates as a forward spectrometer called the Zero Degree Spectrometer (ZDS).

2.3 Zero Degree spectrometer

The Zero Degree Spectrometer (ZDS) is depicted in Fig. 2.1 and consists of two dipoles and 6 STQs starting from the experimental focus F8 to F11. ZDS has a similar layout of

magnets as BigRIPS with momentum-dispersive focal planes at F9 and F10, and a fully achromatic final focus F11. The quadrupole magnets (STQ15 and STQ16) in the section connecting BigRIPS and ZDS (F7-F8) ensure proper focusing ion-optical conditions at F8, where a secondary reaction target is placed. Similarly, STQ20, STQ21, and dipole D8 in sections F9-F11 are adjusted to direct the secondary reaction products to the achromatic focus F11, where the carbon reaction target $(2.5\ g/cm^2)$ was placed for the σ_{cc} measurement. The ZDS is fixed at zero degree for secondary reaction studies with RI beams, and it identifies and analyzes the projectile fragments after the secondary target at F8 using a particle identification scheme similar to the BigRIPS separator, based on TOF $- B\rho - \Delta E$, with trajectory reconstruction.

2.4 Measurement of mass-to-charge ratio

Fig. 2.2 displays the utilization of the BigRIPS separator to separate the secondary beams. The mass-to-charge ratio is determined through the Lorentz equation (Eq. 2.1), which explains the motion of charged particles in uniform magnetic fields generated by dipoles:

$$F = qvB = \frac{mv^2}{\rho} = \frac{\gamma m_0 v^2}{\rho} \tag{2.1}$$

where q is the ionic charge state of the fragment, B is the magnetic field in the dipole, ρ is the radius of the trajectory, m_0 is its rest mass, and $\gamma = \frac{1}{\sqrt{1-\beta^2}}$ is the relativistic factor with $\beta = v/c$ (c is the speed of light). Eq. 2.1 can be rearranged as,

$$\frac{m_0}{q} \approx \frac{A}{Z} = \frac{B\rho c}{u\beta\gamma} \tag{2.2}$$

where u is the atomic mass unit equal to $931.494\,\mathrm{MeV/c^2}$ and the charge equal to Z as the nuclide of interest is fully stripped. The product $B\rho$ is the magnetic rigidity (χ) of a

beam, a parameter defined as following,

$$\chi = B\rho = \frac{p}{q} \tag{2.3}$$

where p and q are the momentum and charge of the particle, respectively. In a magnetic field, the particle with greater momentum will experience less bending as it moves through the field. The variable χ is inversely proportional to the particle's charge, meaning that particles with higher atomic numbers (Z) will experience greater bending as they travel through the magnetic field.

The BigRIPS and ZDS are designed to operate in the dispersion-matched mode, where the dispersion of the first stage is compensated by the dispersion of the second stage. For a specific A/Z fragment, the χ value of the F0-F1 (dispersive focal plane) and F2-F3 (achromatic focal plane) is configured to converge the fragment back to the same horizontal position, as illustrated in Fig. 2.3.

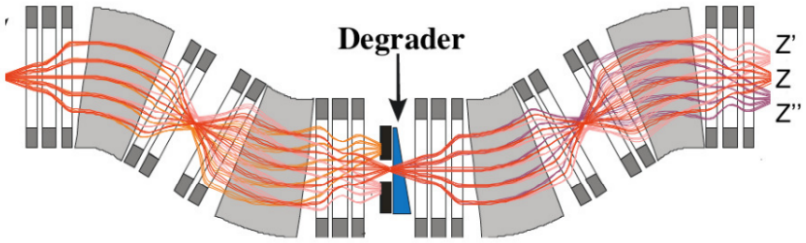

Figure 2.3: Schematic view of ion-optics on passing through a degrader [23].

A technique known as the momentum-loss achromat is utilized to separate the fragments in flight by inserting **wedge-shaped** energy degraders at the experimental foci F1 and F5. This is done by taking advantage of the fact that the energy loss of particles is proportional to Z^2/v^2, which causes isotopes to have different velocities as they pass through the degrader. This results in fragments with the same A/Z being separated in position, as shown in Fig. 2.3.

The setup maintains its achromaticity due to the wedge-shaped design of the degrader. Higher velocity fragments pass through more degrading material, while lower-velocity fragments pass through less. Additionally, the presence of slits at F0 helps to reduce contaminants from the reaction, as shown in Fig. 2.2.

2.5 Experimental Methodology

As previously stated, the charge-changing cross-section (σ_{cc}) for reactions that alter the proton number of the projectile nucleus was determined using the transmission method on a carbon target. The number of incident nuclei was identified and counted based on their total mass and proton number (^{A}Z) on an individual event basis before the reaction takes place. The nuclei that pass through the reaction target at F11 with charge $\geq Z_{incident}$ are identified and counted.

The intensity of the beam particles diminishes as they interact with matter. The reaction cross-section (σ_R) measures the nuclide-changing reactions, where the number of collisions per unit time per unit area is then proportional to the number of incident particles N_{in} and the number of target particles. The reaction cross-section is defined as [67]:

$$N = N_{in} e^{-\sigma_R t} \tag{2.4}$$

where N is the number of particles unreacted after passing through the target, and t is the number of target nuclei per cm^2. Analogous to the reaction cross-section, σ_{cc} is defined as:

$$N_{in} - N_Z = N_{in} e^{-\sigma_{cc} t} \tag{2.5}$$

Here, N_Z denotes the number of particles per unit time that undergo a charge-changing reaction. $N_{in} - N_Z$ consequently corresponds to the number of particles that emerge with unchanged charge which can be denoted as $N_{out \geq Z}$. Hence the σ_{cc} can be written

as,

$$\sigma_{cc} = -\frac{1}{t} \ln \frac{N_{out \geq Z}}{N_{in}} \tag{2.6}$$

It is important to note that nuclear reactions may occur in the non-target materials within the beamline. To account for this effect, measurements are taken without the target in the setup. As a result, the charge-changing cross-section (σ_{cc}) can be represented as,

$$\sigma_{cc} = \frac{1}{t} \ln \frac{R_{Tout}}{R_{Tin}} \tag{2.7}$$

The transmission ratio with the reaction target (R_{Tin}) can be expressed as $R_{Tin} = N_{out \geq Z} / N_{in}$ and R_{Tout} denotes the transmission ratio without the reaction target. The main advantage of this method is that it involves event-by-event counting of the selected incident beam, thus eliminating uncertainty in selecting the incident particles (N_{in}) of the desired isotope.

2.6 Experiment setup at BigRIPS

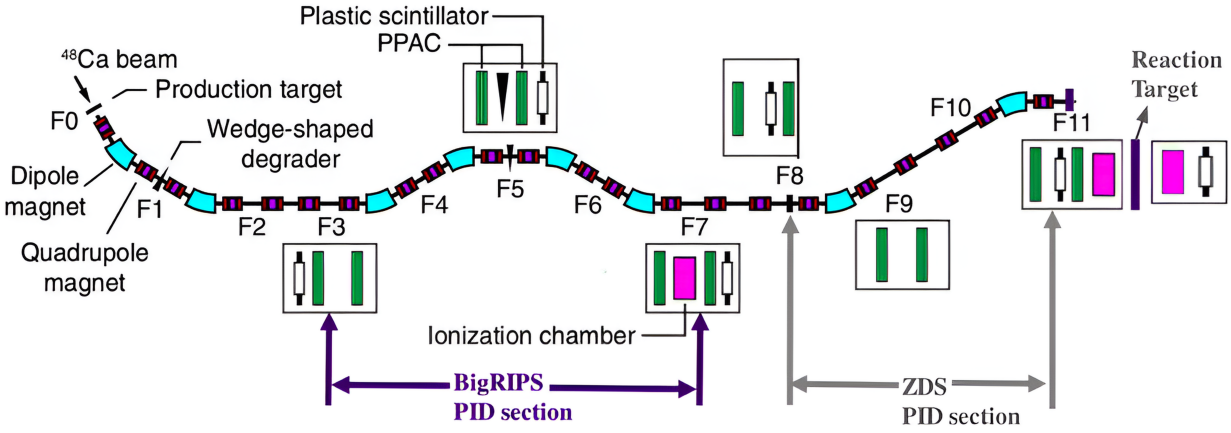

Figure 2.4: Schematic view of experimental setup [68].

The exotic nitrogen isotopes were created by fragmenting a ^{48}Ca beam with a 570 pnA intensity and 345A MeV energy, which interacted with a 10 mm rotating Be target. The

BigRIPS separator was used to separate the isotopes of interest from the contaminants and identify them using in-flight energy deposit (ΔE), time of flight (TOF), and magnetic rigidity ($B\rho$). Aluminium degraders of 15 mm and 5 mm thicknesses were placed at dispersive foci F1 and F5 [black inverted triangles in Fig. 2.4] to separate the beam contaminants spatially. The magnetic rigidity determination requires the x position of RI beams, therefore each focal plane is equipped with two sets of position-sensitive parallel plate avalanche counters (PPAC) [green boxes in Fig. 2.4]. A multi-sampling ionization chamber (MUSIC) at F7 and F11 [pink boxes in Fig. 2.4] provided ΔE information, while plastic scintillator detectors [transparent boxes in Fig. 2.4] of 3mm thickness at focal planes F3, F7 and F11 provided TOF information. A schematic view of the experimental setup with these detectors is shown in Fig. 2.4. MUSIC detectors are placed before and after a 2.5 g/cm^2 thick carbon reaction target. The following sections outline the key characteristics of the detectors employed in the experiment.

2.6.1 Multiple-Sampling Ionization Chamber (MUSIC)

As previously mentioned, the Z of the incident particles and reaction products at F11 is determined through the measurement of ΔE, using two multiple-sampling ionization chambers (MUSIC) based on the design described in [69]. These MUSIC detectors were from GSI in Germany. The ionization chamber utilized in the experiment consists of eight anodes, which are made of a thin foil of mylar coated with aluminum on both sides. A schematic view of the internal geometry is shown in Fig. 2.5. The active length of the ionization chamber along the beamline is 400 mm, and the anodes are electrically paired and connected together. The ionization chamber is filled with CF_4 gas and operates at room temperature and atmospheric pressure. The ionizing particles lose energy as they pass through the gas, generating electron-ion pairs. The amount of electrons produced is proportional (to a first order approximation) to the square of the charge of the penetrating particle. The energy loss of charged particles in a material is

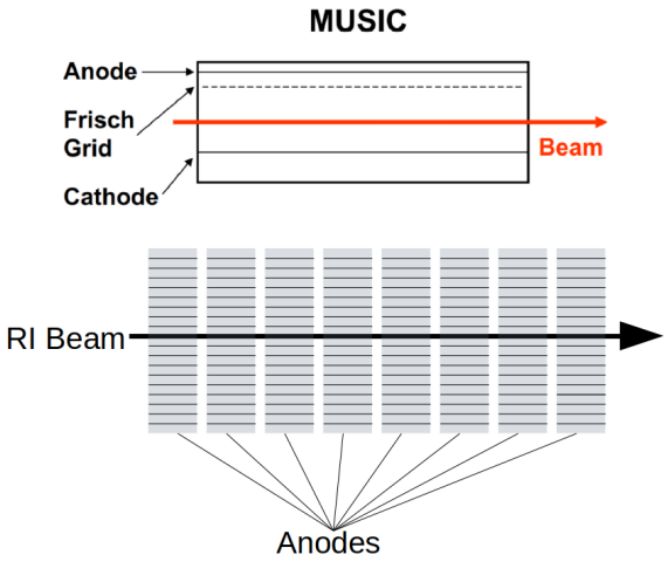

Figure 2.5: Schematic view of ions passing through the MUSIC detector.

described by the Bethe-Bloch formula:

$$-\frac{dE}{ds} = \frac{4\pi Z_p^2}{m_e c^2 \beta^2}\left(\frac{e^2}{4\pi\epsilon_0}\right)^2 Z_t N_t \left(\ln\frac{m_e v^2}{I} - \ln(1-\beta^2) - \beta^2\right) \tag{2.8}$$

where s denotes the path length of the particle in the absorber, Z_p and β correspond to the charge and the velocity of the penetrating particle. Z_t, N_t and I are the proton number, the particle density and the mean excitation potential of the material, respectively. Finally, e and m_e are the charge and mass of the electron [70]. Electrons move towards segmented anodes in an electric field and are collected there. Their charge is then transformed into a proportional signal amplitude by charge-sensitive pre-amplifiers. To determine the charge information, the geometric average of the signals from eight anodes is calculated.

2.6.2 Parallel Plate Avalanche Counter (PPAC)

The X and Y positions of each beam event were determined using Parallel Plate Avalanche Counters (PPACs) [71] installed at each focal plane for trajectory reconstruction. PPACs,

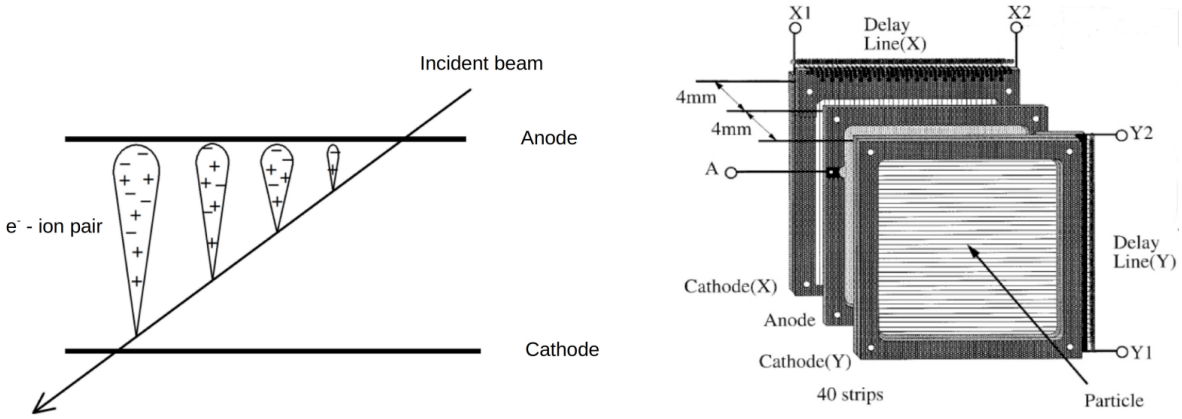

(a) Operating principle of PPAC. **(b)** An enlarged view of the delay-line PPAC

Figure 2.6: Schematic and operating principle of a PPAC in BigRIPS [71].

with a material thickness of only 30 mg/cm^2, have an extremely small impact on energy loss in the beam path, in contrast to other position-sensitive detectors like multi-wire proportional counters and multi-wire drift chambers. The lack of wires in PPACs, a gas detector, further minimizes obstacles in the transport of RI beams. PPACs are also durable and easy to maintain because of their simple design, and use a delay-line readout technique for position determination, providing high $B\rho$ resolution for particle identification. This not only facilitates RI beam production and transport but also supports beam diagnostics for BigRIPS and ZDS.

The delay-line PPAC consists of electrode strips connected to a multi-tapped delay line and position information is obtained from the time difference between signals from either end. The anode electrode is sandwiched between two cathode electrodes (one for the x-axis and one for the y-axis) with strip widths of 2.4 mm and inter-spacing of 0.15 mm. When a 1500 V bias voltage is applied between the electrodes, induced electrons from incident ions undergo a Townsend Avalanche. The counter gas, such as isobutane (C_4H_{10}) or perfluoropropane (C_3F_8), is used at a pressure of 3-50 Torr. When heavy ions pass through the detector, they immediately create electron-ion pairs, resulting in an electron avalanche (as shown in Fig. 2.6a) and a signal with excellent timing properties

(rise and fall times of a few ns). This is a significant improvement over proportional counters, which have a time delay before the electron shower occurs. As mentioned earlier, each PPAC is comprised of two planes sensitive to position and angle in the X direction and two planes segmented in the Y direction (Fig. 2.6b). The time-to-digital converter (TDC) measures the delay time, which begins with the anode signal (electron drift time) and ends with cathode signals. The fast induced signals in the cathode enter the delay line and travel to the $X1$ and $X2$ cathode terminals on the left and right, respectively. The delay time in the cathode terminals is expressed as T_{X1} (ns) and T_{X2} (ns), and the position of the ionizing particle, X_{Pos}, is calculated as follows:

$$X_{Pos} = K_X \times \left(\frac{T_{X1} - T_{X2}}{2} \right) + X_{off} \tag{2.9}$$

where K_X (mm/ns) and X_{off} (mm) are the position coefficient and the offset correction, respectively. The control sum is the sum of the total delay time which corresponds to the total delay line length.

$$T_{sumX} = T_{X1} + T_{X2} - 2T_a \tag{2.10}$$

Similarly, Y_{Pos} and T_{sumY} are computed for the Y position. The control sum is a constant value for normal events, as it is independent of the position of the ionizing particle. However, if the avalanche region expands due to the production of $\delta-$rays or multiple hits, the control sum decreases as T_{X1} and T_{X2} become smaller than the normal value [71].

2.6.3 Plastic Scintillators

Plastic scintillators are solid materials made of a polymer matrix mixed with a luminophore that emit light when exposed to ionizing radiation. They are commonly used in nuclear physics experiments to measure the time-of-flight (TOF) [72]. The work-

ing principle of plastic scintillators in detecting exotic nuclei is based on the interaction of ionizing radiation with the material. The scintillation mechanism in organic materials is unique, as it results from the arrangement of the crystal lattice (Fig. 2.7). When a high-energy particle passes through the plastic scintillator, it ionizes the molecules,

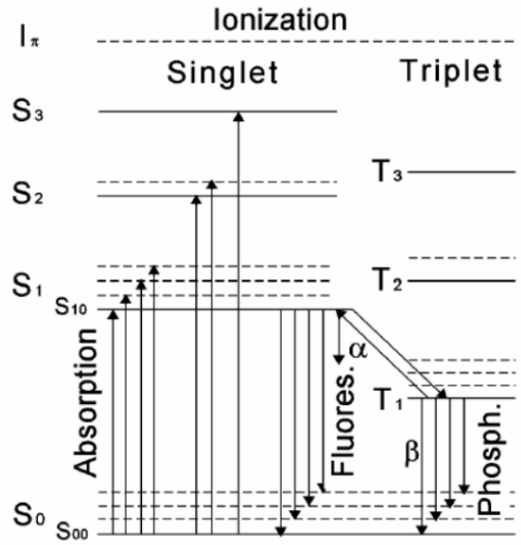

Figure 2.7: Energy levels of organic molecules.

causing the luminophore to emit light. This light is then detected by Photo-Multiplier Tubes (PMT) or other types of light detectors. Plastic scintillators are popular in exotic nucleus research due to their high efficiency, a short decay time ($\sim$ 2 ns), low cost, and relatively small size compared to other types of radiation detectors.

In the BigRIPS and ZDS setup, the plastic scintillator detectors utilized were the EJ-212 and EJ-230 from Eljen Technology. The setup utilized Hamamatsu PMTs (H6533 and H2431 models) connected to both ends of the plastic scintillator in the horizontal direction. The difference in time between the signals from these two PMTs provides information about the position of the incoming particle. The PMT outputs serve as the start and stop signals for the time-to-digital converters (TDC), and the average of the two timing signals from each PMT is used as the final time-of-flight (TOF) measurement to eliminate any time differences due to different hitting positions. The signals from the plastic scin-

tillation detectors are split into two; one is fed to a Charge-to-Digital Converter (QDC) for energy loss measurement and the other to a Leading Edge Discriminator (LED) with a threshold set above the PMT noise level.

2.6.4 Veto Scintillator

Veto scintillators are typically positioned around the reaction area to help reject or "veto" unwanted events. A veto scintillator was placed in front of the carbon reaction target at F11. The aperture of the veto scintillator is smaller than the reaction target area, with two PMTs connected on its right side and left side. The readout from these PMTs is used to identify signals generated by charged particles passing through the scintillator. The goal is to reject signals generated by particles near the edge of the reaction target, as well as those produced by nuclear reactions along the beamline upstream. Therefore, in the process of offline data analysis, signals detected by either PMTs are excluded from the incident beam selection for the specific isotopes of interest (Fig. 2.8), thereby improving the accuracy of its identification. The impact of these events (events identified by veto

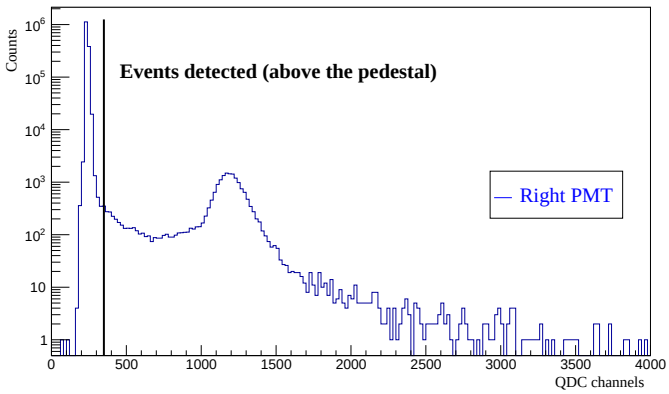

Figure 2.8: Energy deposited in the right PMT of the veto scintillator with the incident ^{23}N beam. A comparable spectrum has been observed for the left PMT.

detectors) on the measured charge changing cross-section will be elaborated upon in the concluding chapter.

Chapter 3

Data analysis

This chapter provides an overview of the techniques employed to extract the physical observables of interest from the detectors. The raw data collected from the detectors are in a digitized form, for example in ADC and TDC. Performing detector calibration of these TDCs and ADCs, we can convert the digital signal into a physical quantity like time, charge, and energy. In the first few sections, calibration procedures of all the detectors are discussed. Once the detectors are calibrated, the data analysis is divided into two essential parts. The first part involves particle identification (PID) before the reaction target for incident beam selection, while the second part focuses on identifying charge-changing events after the reaction target, both of which are crucial for determining σ_{cc}. The phase space restriction on the incident beam particles is discussed in detail in this chapter.

3.1 Z identification

The atmic number Z of the incident particles and reaction products at F11 is determined through the measurement of ΔE, using two multiple-sampling ionization chambers (MUSIC) placed before (MUSIC1) and after (MUSIC2) the carbon target at F11. The ionization chamber used in the experiment consists of eight anodes, which are made

of a thin foil of mylar coated with aluminum on both sides. The charged particle deposits energy as it passes through the detector material, which generates a voltage pulse.

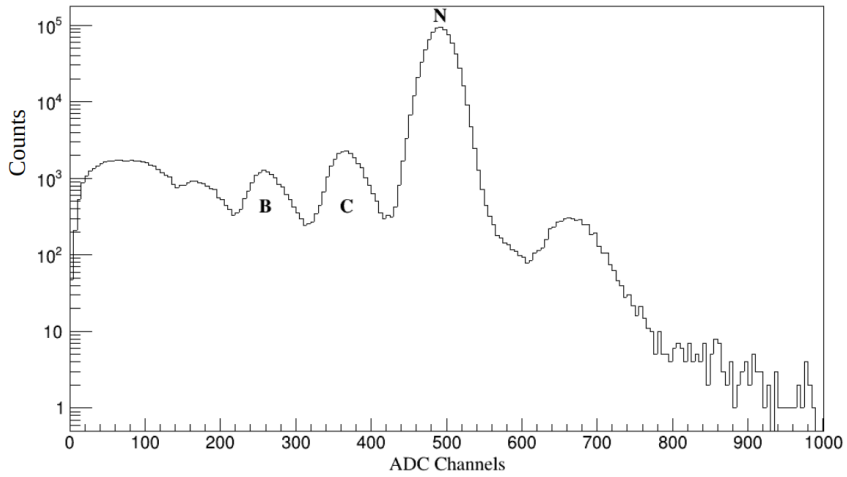

(a)

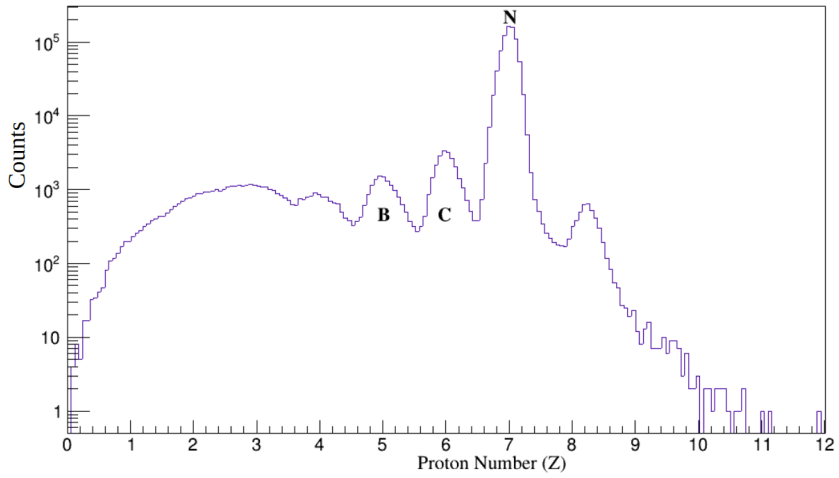

(b)

Figure 3.1: (a) The geometric average of the uncalibrated MUSIC (ADC channels) spectrum. (b) The calibrated Z spectrum.

The voltage pulse is initially transformed into a channel number using a peak-sensing ADC. Calibration, in this context, involves converting this channel number into a more meaningful physical measurement, specifically energy loss. For individual anodes in the MUSIC detector, pedestal subtraction is performed first, followed by gain matching to ensure consistent gains by aligning their respective channel numbers. This alignment

process is achieved by applying a multiplication factor 'g' that corresponds to the peak position (channel) of the central anode, as described by the given equation,

$$E_c = (C - P) \times g \tag{3.1}$$

where C represents the channel numbers from the ADC, pedestal P is the zero-energy point in the ADC spectrum, and g is the factor used for gain matching of the anodes. To convert the pedestal-subtracted, gain-matched ADC channel numbers (E_c) (see Fig. 3.1a) into a physical quantity, namely atomic number (Z) (see Fig. 3.1b), the geometric mean of eight such E_c values is calculated. This geometric mean is then used to determine Z as the stopping power $(-\frac{dE}{dx})$ is directly proportional to $\frac{Z^2}{\beta^2}$, where β represents the velocity of the incident particle:

$$Z = \sqrt{\text{Geometric Mean of anodes}} \times \beta \tag{3.2}$$

Z obtained in this way for neighboring elements is then matched with their actual Z value, i.e., $Z = 5, 6, 7$, to obtain the offset correction. The decision to use the geometric mean for the anodes was based on its superior resolution compared to the arithmetic mean of the anodes. The Z resolution for ^{23}N is determined to be 0.18, represented by the Full Width at Half Maximum (FWHM) (Fig. 3.1b).

3.2 Position determination

The determination of the X and Y position of each beam event is a critical aspect for particle identification, and we achieve this using double PPACs strategically placed at each focal plane for trajectory reconstruction. As discussed in 2.6.2, the delay-line PPAC comprises electrode strips connected to a multi-tapped delay line. Essential position information is derived from the time difference between signals received from either end

of the delay line. When one side of the PPAC detects an event or "hit", this information is utilized to figure out where the incident beams are positioned in both the horizontal (X) and vertical (Y) directions at various focal planes in the experimental setup. The process of track reconstruction is conventionally split into two steps: track finding and track fitting. Track finding involves grouping together hits that come from the same events, creating subsets of information. With these subsets, we can optimally estimate a set of track parameters from the hit information. The track fitting step utilizes a mathematical technique called least square minimization. For optimal tracking performance, the system requires specific hit configurations. Ideally, either all four planes from both PPACs (Fig.3.2a) or a minimum of three out of the four planes from the double PPACs, positioned upstream and downstream of the focal planes (Fig.3.2b), should register hits. This condition proves crucial in significantly minimizing tracking errors. Furthermore, tracking initiation mandates at least one hit in the planes of the upstream PPAC and one hit in the planes of the downstream PPAC (Fig.3.2c). This requirement ensures the robustness and reliability of the tracking process.

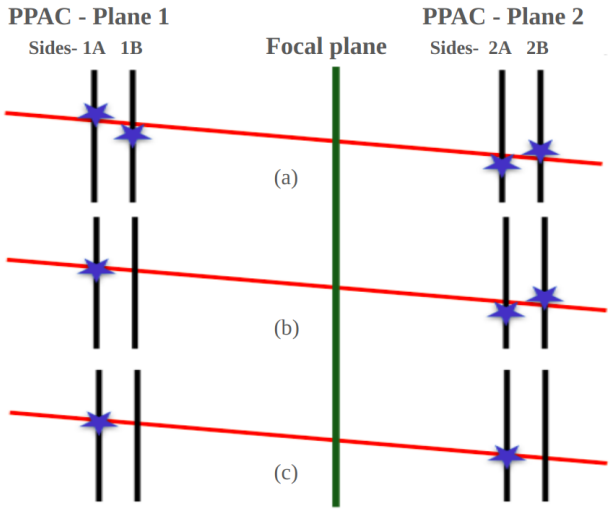

Figure 3.2: Diagram illustrating two PPACs and the distribution of 'hits' across their planes at the experimental focal point.

The least square minimization technique yields deviations denoted as D^2, computed

on an event-by-event basis using the expression:

$$D^2 = \sum_i [Y_i - (mX_i + c)]^2 \tag{3.3}$$

Here, the subscript i corresponds to the side of the PPAC plane, as illustrated in Fig. 3.2. These deviations are minimized between the model $(c + m \times X_i)$ and the actual data Y_i, facilitating the determination of trajectories at the focal planes with high precision. Fig. 3.3 shows the X and Y profile of the beam at the final focal plane (F11) with ^{21,23}N secondary beam selection.

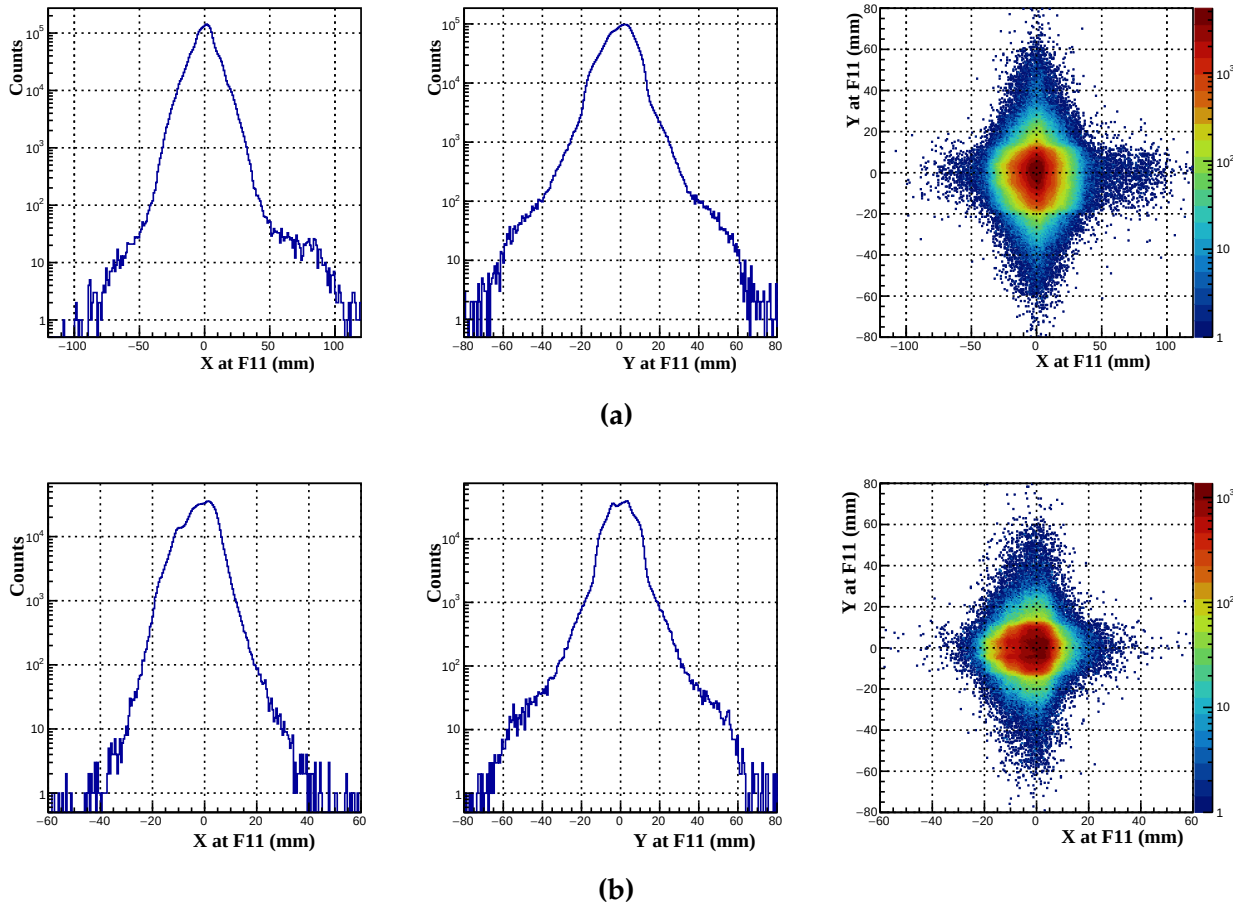

Figure 3.3: Beam profile at F11 with (a) ^{23}N secondary beam selection and (b) ^{21}N secondary beam selection.

3.3 Time of flight measurement

The time-of-flight (TOF) measurement of the Radioactive Ion (RI) beams is conducted using plastic scintillators positioned at different focal planes (F3, F5, F7, F8, F11). Specifically, in the BigRIPS and ZDS setup, the plastic scintillator detectors employed are the EJ-212 and EJ-230 models from Eljen Technology. The setup incorporates Hamamatsu Photomultiplier Tubes (PMTs), specifically the H6533 and H2431 models, connected to both ends of the plastic scintillator along the horizontal direction.

To account for time variations resulting from incoming particles striking different positions on the plastic scintillator, the average of the two timing signals recorded from both sides of the PMT is determined. Let TL and TR represent the time recorded at the left and right sides, respectively. The average time, denoted as T_{Avg}, is calculated as:

$$T_{\text{Avg}} = \frac{TL + TR}{2} \tag{3.4}$$

The time-averaged signal from a single plastic scintillator positioned at a focal plane lacks physical significance; therefore, the TOF between two focal planes is calculated by taking the difference of these averaged values. For instance, the TOF between F11 and F8 (TOF_{811}) is given by:

$$TOF_{811} = (T_{\text{Avg}} \text{ at } F11 - T_{\text{Avg}} \text{ at } F8) \tag{3.5}$$

Now, considering that $TOF = \frac{L}{\beta c}$, where L represents the flight path between the plastic scintillators positioned at F8 and F11 (36.983 m), and c denotes the speed of light, the relativistic velocity (β) can be calculated using the following equation:

$$\beta = \frac{L}{TOF \cdot c} \tag{3.6}$$

Time of Flight (TOF_{37}) computation has been performed for the path between F3

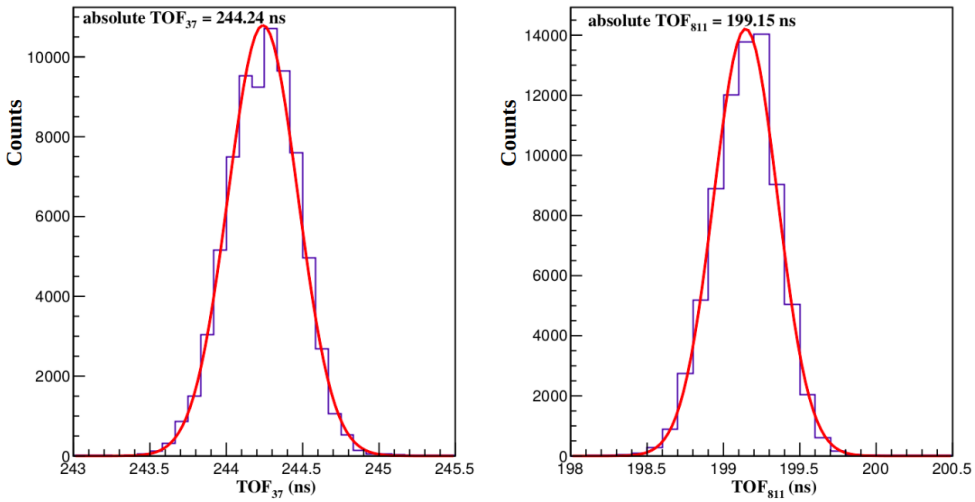

Figure 3.4: Absolute TOF (ns) for the flight path (a)F3 to F7 (b) F8 to F11, of ^{23}N. The red curve represents the fitted Gaussian distribution of the histogram.

and F7, where the distance between the focal planes is 46.978 m. Fig. 3.4 displays the absolute TOF for the central region of ^{23}N secondary beam at dispersive focal plane F5. The absolute TOF is essentially the measured TOF plus the offset correction. This offset correction is determined by comparing the measured TOF with the theoretical TOF calculated for the ^{23}N isotopes using the magnetic field.

A similar time-of-flight analysis has been conducted with the ^{21}N incident beam selection, using the same experimental setup as discussed previously for the ^{23}N case. The path length between F3 and F7, as well as between F8 and F11, remains consistent with the previous analysis. The TOF for the ^{21}N is presented in Fig. 3.5.

3.4 Particle identification

Multiple secondary beam fragments reach the reaction target situated at F11. Thus, the accurate identification of a nucleus, determined by its mass and charge number, plays a crucial role in distinguishing the incident beam of the isotopes of interest (^{21,23}N). The desired isotopes were distinguished from cocktail of fragments through the utilization

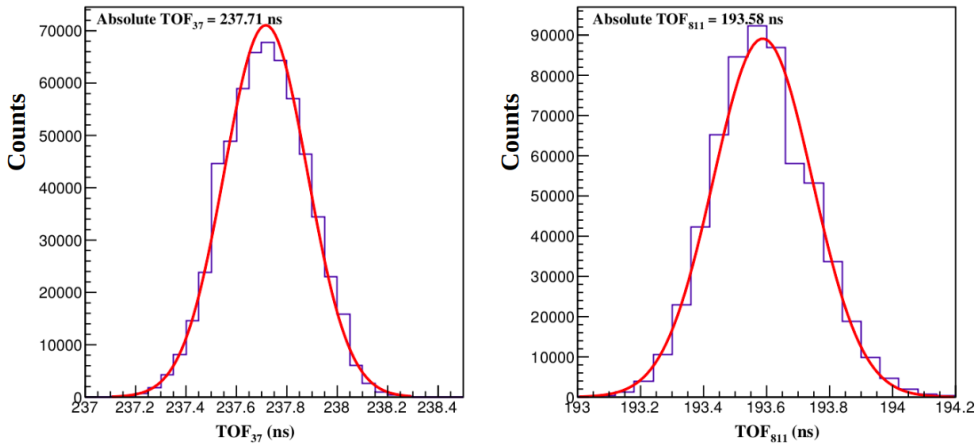

Figure 3.5: Absolute TOF (ns) for the flight path (a)F3 to F7 (b) F8 to F11, of ^{21}N. The red curve represents the fitted Gaussian distribution of the histogram.

in the BigRIPS fragment separator, and their identification was accomplished employing the methods of in-flight energy deposit (ΔE), time of flight (TOF), and magnetic rigidity ($B\rho$). The measurement of energy deposition in the MUSIC detectors yields the atomic number (Z) for fully ionized heavy ions. The mass number is subsequently obtained from the mass-to-charge ratio, described by the motion of Radioactive Ion (RI) beams within the magnetic field. As discussed in Eq. 2.3, magnetic rigidity is essentially the ratio of momentum to charge. The fractional momentum deviation (δ) is computed from the deviation from the central trajectory ($B\rho_0$). The $B\rho$ value of the fragments on the central trajectory ($B\rho_0$) was determined using the magnetic fields of the dipoles with NMR probes during the experiment.

$$\delta = \frac{p - p_0}{p_0} = \frac{B\rho - B\rho_0}{B\rho_0} \quad (q = q_0) \tag{3.7}$$

The dispersion matching of two stages requires that the deviation in the horizontal position of the first stage (F3–F5) is compensated by the (F5–F7) dispersion ($x|\delta$) of the second stage in BigRIPS and in the ZDS the dispersion matching sections are F7–F9 and F9–F11. The momentum spread of the fragment ($+\delta$ and $-\delta$) is dispersed in position at the dispersive focus (F5 in BigRIPS and F9 in ZDS), while the angular spread is focused

back to a point. Therefore, the position in x at the dispersive focus only depends on the fractional momentum deviation δ. δ can be derived with the first-order ion optical transfer matrix M [73]:

$$\begin{bmatrix} X_j \\ A_j \\ \delta_{ij} \end{bmatrix} = \begin{bmatrix} (x|x) & (x|a) & (x|\delta) \\ (a|x) & (a|a) & (a|\delta) \\ (\delta|x) & (\delta|a) & (s|\delta) \end{bmatrix} \begin{bmatrix} X_i \\ A_i \\ \delta_{ij} \end{bmatrix} \tag{3.8}$$

Here, x and a represent horizontal position and angle, and s is the distance along the central trajectory. Subscripts i and j denote upstream and downstream focal plane information respectively. As previously mentioned, the horizontal position (x) remains unaffected by the initial angle in a system employing point-to-point imaging. Consequently, the matrix element in 3.8 $(x|a)$ is zero. Hence, the derived quantity δ_{ij} for all particles is expressed as:

$$\delta_{ij} = \frac{1}{(x|\delta)_{ij}} \left[X_j - (x|x)\ X_i \right] \tag{3.9}$$

For, focal plane F5 and F7 in BigRIPS set up, the Eq. 3.9 can be re-written as:

$$\delta_{57} = \frac{1}{(x|\delta)_{57}} \left[X_7 - (x|x)\ X_5 \right] \tag{3.10}$$

Eq. 3.7 is rearranged to express the magnetic rigidity as:

$$B\rho = (1 + \delta_{57}) B\rho_0 \tag{3.11}$$

To incorporate energy loss, a dual $B\rho$ measurement, coupled with time-of-flight (TOF) measurements, is utilized. The TOF measurement between plastics (F7–F3) de-

termines the A/Q value of fragments:

$$\begin{aligned} \text{TOF} &= \frac{L_{35}}{\beta_{35}c} + \frac{L_{57}}{\beta_{57}c} \\ \left(\frac{A}{Q}\right)_{35} &= \frac{B\rho_{35}c}{\beta_{35}\gamma_{35}m_u} \\ \left(\frac{A}{Q}\right)_{57} &= \frac{B\rho_{57}c}{\beta_{57}\gamma_{57}m_u} \end{aligned} \tag{3.12}$$

Subscripts 35 and 57 denote the F3–F5 and F5–F7 sections in the BigRIPS, respectively. If there is no alteration in A/Q (Q $\sim$ Z, as the ions are fully stripped) in Eq. 3.12, then:

$$\frac{\beta_{35}\gamma_{35}}{\beta_{57}\gamma_{57}} = \frac{B\rho_{35}}{B\rho_{57}} \tag{3.13}$$

Using the measured TOF and magnetic rigidity, fragment velocities before (β_{35}) and after (β_{57}) the wedge degrader at the dispersive focal plane (F5) can be deduced. The absolute A/Z value is determined using:

$$\frac{m_0}{q} \approx \frac{A}{Z} = \frac{B\rho_0 c}{u\beta\gamma}(1+\delta_{57}) \tag{3.14}$$

The absolute Z value derived from the energy loss in the MUSIC detector is vital for particle identification. Therefore, with the absolute values of Z and A/Z, particle identification can be accomplished. A similar methodology is employed to achieve Particle IDentification (PID) at the final focal plane position (F11), particularly relevant for measuring charge-changing cross sections. This involves utilizing track information obtained from double position-sensitive PPAC detectors located at F9 and F11. The magnetic rigidity ($B\rho$) of fragments along the central trajectory is determined using a method analogous to that used for BigRIPS, involving the measurement of magnetic fields of the dipoles through NMR probes. At F11, the A/Z ratio is determined using the same technique as

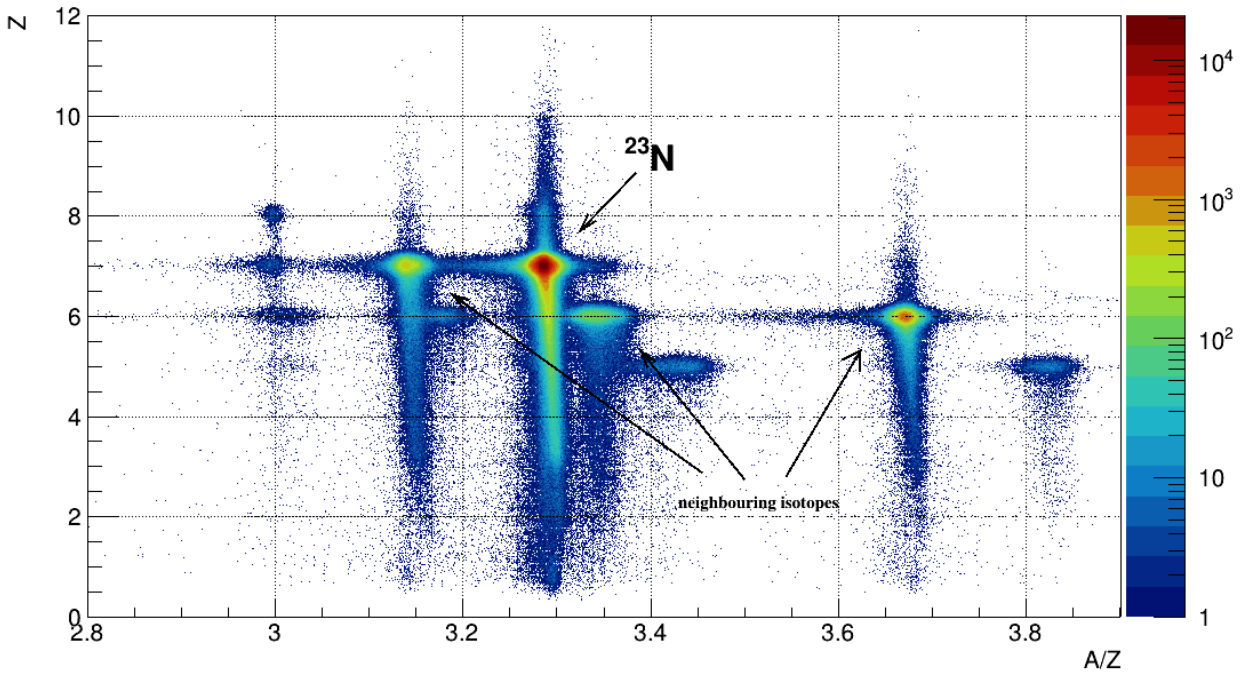

Figure 3.6: Particle identification plot for ^{23}N fragments from a ^{48}Ca primary beam in BigRIPS at F11 (without any cleaning conditions). The color bar represents the number of events on the z-axis (in log scale).

explained for A/Z at F7:

$$\frac{A}{Z} = \frac{B\rho_0 c}{u\beta\gamma}(1+\delta_{911}) \tag{3.15}$$

Here, $B\rho_0$ represents the magnetic rigidity on the central trajectory, and δ_{911} accounts for the fractional momentum deviation. With the absolute values of A/Z and Z obtained from the MUSIC detector, Particle IDentification (PID) can be achieved at F11 before the target (Fig. 3.6). The neighbouring isotopes such as ^{22}N and ^{20}C are clearly observable in close proximity to the ^{23}N secondary beam, as illustrated in Fig. 3.6.

Using a technique identical to the one employed for the identification of ^{23}N events, the ^{21}N events are also identified based on magnetic rigidity (Bρ), time-of-flight (TOF), and energy-loss (ΔE)(Fig. 3.7) information. The PID plot in Fig. 3.7 reveals the presence of ^{21}N along with its neighboring isotopes, $^{18-20}$C and ^{20,22}N.

The selection of incident beam for both ^{21,23}N requires a careful analysis of the position and angular correlations of the secondary beam detected by detectors positioned at

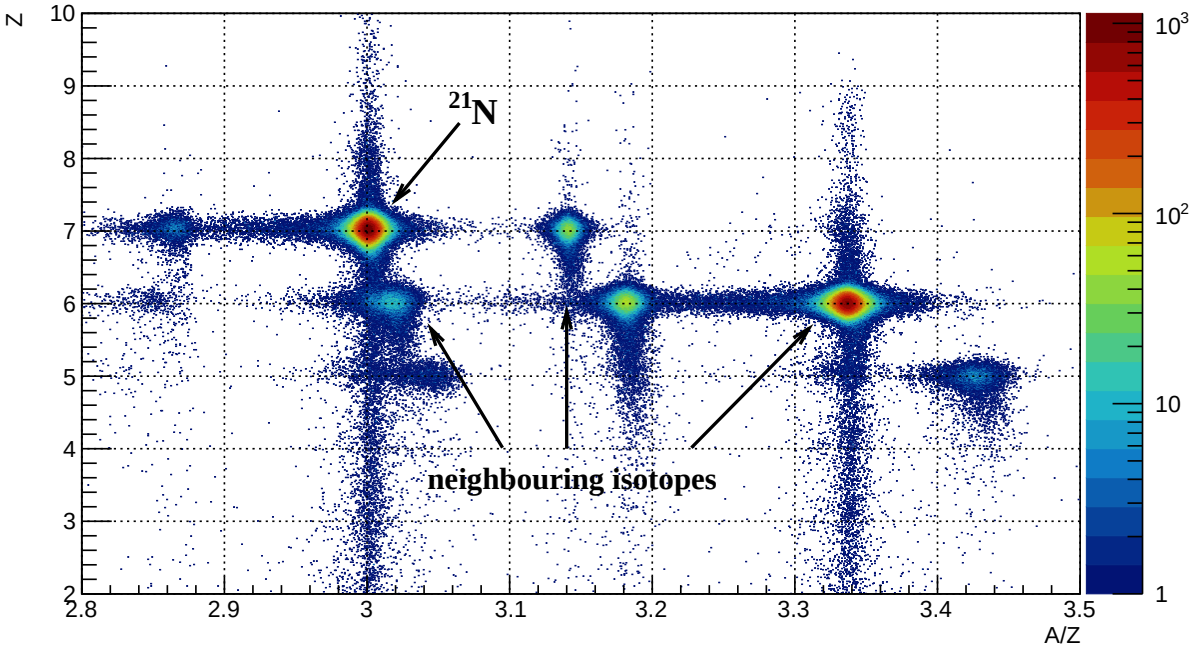

Figure 3.7: Particle identification plot for ^{21}N fragments from a ^{48}Ca primary beam in BigRIPS at F11 (without any cleaning conditions). The color bar represents the number of events on the z-axis (in log scale).

different focal planes upstream of the carbon target at F11. This process is essential for filtering out spurious events, and a detailed discussion of this matter will follow in the subsequent section.

3.5 Incident beam selection

As discussed in 2.5, the charge-changing cross-section is obtained by counting the number of incident beam particles (N_{in}) and the particles with unchanged charge (Z) (N_{sameZ}). The charge-changing cross-section (σ_{cc}) can be represented as,

$$\sigma_{cc} = \frac{1}{t} \ln \frac{R_{Tout}}{R_{Tin}} \tag{3.16}$$

The transmission ratio with the reaction target (R_{Tin}) and without the reaction target

(R_{Tout}) is $N_{out\geq Z}/N_{in}$. The main advantage of this method is that it involves event-by-event counting of the selected incident beam, thus eliminating uncertainty in selecting the incident particles (N_{in}) of the desired isotope.

3.5.1 ^{23}N incident beam selection

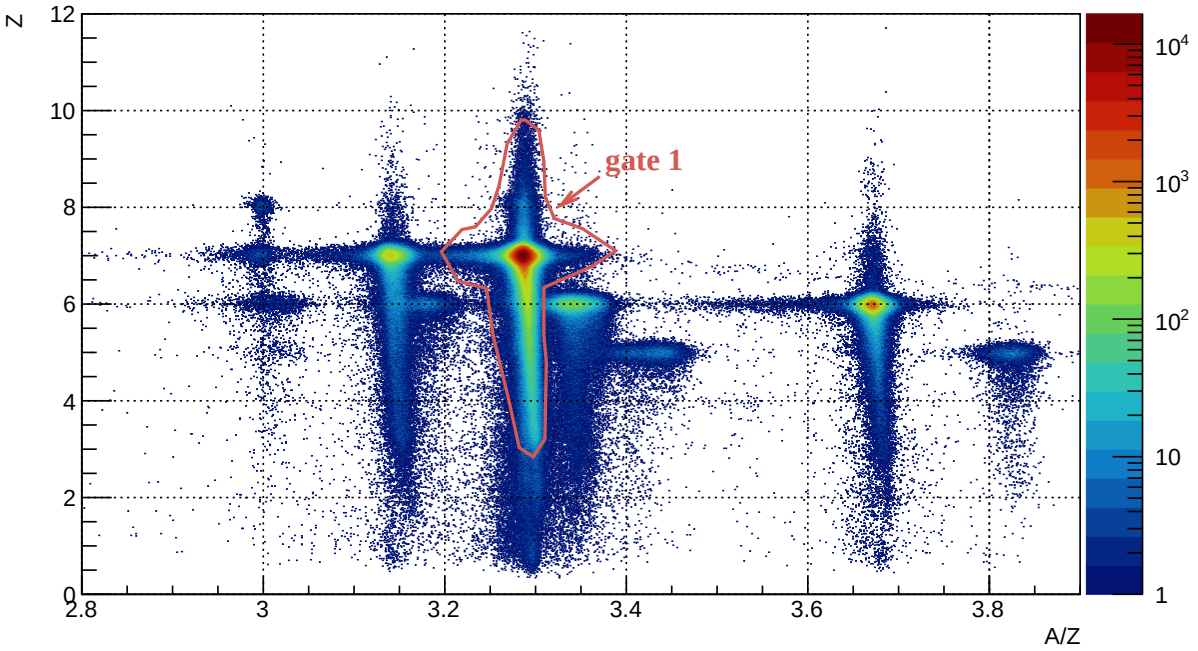

Figure 3.8: PID at F11 before target. The geometric cut (*gate 1*) represents the extended selection of ^{23}N.

The primary objective of incident beam selection is to minimize the impact of spurious events while preserving essential statistical data by analyzing position and angle correlation plots at various focal planes ranging from F5 to F11 before reaching the target. Upon thorough analysis of various correlation plots and their influence on the Z spectrum after the reaction target, several graphical events selections (referred to as *gates*) have been implemented in the detectors placed before the reaction target. Major concerns arise regarding the background events of lower Z along A/Z = 3.3, as depicted in the PID plot shown in Fig 3.6. Therefore, an extended gate of ^{23}N was made (*gate 1*

in Fig. 3.8) to investigate the origin of these events. This tail can be partially removed after examining the correlation between the vertical position (Y at F11) of the selected beam at F11 and the atomic number (Z) derived from the MUSIC detector placed before the target. The events within the tail portion of the correlation plot (Fig. 3.9) have

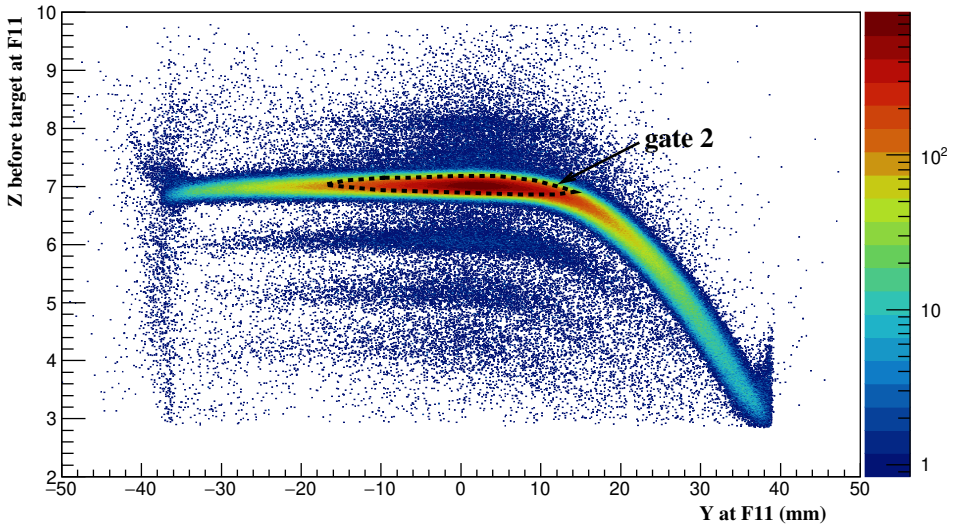

Figure 3.9: Correlation plot between Z before the target at F11 and the vertical position (Y) from MUSIC before the target at F11 with extended ^{23}N (*gate 1*) selection.

been discarded, and only the central region of the correlation plot (*gate 2* in Fig. 3.9), i.e restricting the Y position at F11, has been selected for the incident beam selection. The reason behind this tail-like structure could not be established, but it is believed to be a detector artifact. Even after this tail rejection, another comparable tail-like correlation has been noticed with *gate 1* and *gate 2* between the *Z* after the reaction target and the vertical position (Y from MUSIC2), acquired from the MUSIC detector positioned beyond the target at F11 (Fig. 3.10).

However, unlike the previous issue with the tail-like structure, it cannot be resolved through graphical cuts to eliminate events. Therefore, an investigation was conducted into the origin of these events within the tail-like structure before the target placed at F11. It was observed that, by filtering out events based on the vertical position (Y9) at the F9 focal plane, the tail-type structure can be effectively removed without a substantial

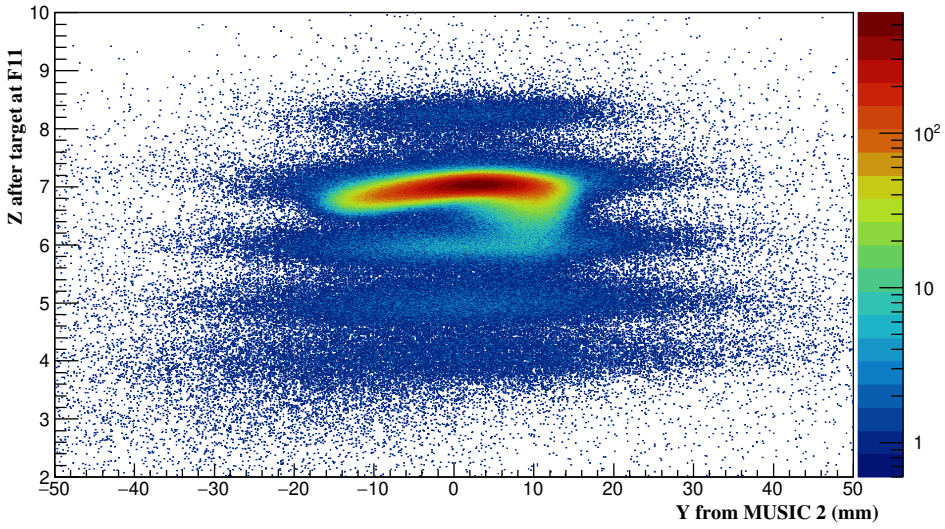

Figure 3.10: Correlation plot between Z after the target at F11 and the vertical position (Y from MUSIC2) for ^{23}N with *gate 1* and *gate 2* (Target-in files).

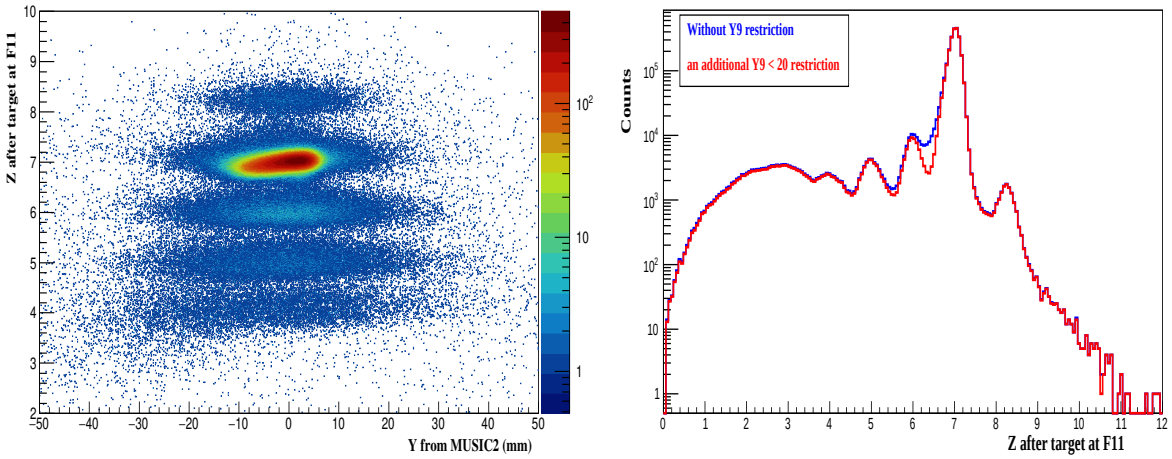

Figure 3.11: Left: Correlation plot between Z after the target at F11 and the vertical position (Y from MUSIC2) for ^{23}N with *gate 1*, *gate 2* and Y9 restriction (target-in files). Right: The effect of the Y9 restriction (Y9 $<$ 20) on the Z spectrum after the reaction target with ^{23}N incident beam selection.

loss in statistics, resulting in an approximate 11% reduction in statistics. The same event selection cuts have also been applied to target-out setup files for consistency in incident beam selection.

Fig. 3.11 shows the correlation plot between the *Z* after the reaction target and vertical

position (Y from MUSIC2) with the mentioned restrictions. It can be observed that the tail-type feature around the Y = 10 mm region (Fig. 3.10) has been significantly reduced in Fig. 3.11, essentially improving the separation between Z = 6 and Z = 7 after the F11 carbon target. The importance of this separation will be discussed in the following sections. It should also be noted that, during the incident beam selection process, events with ADC overflow in the MUSIC detector located before the target have been filtered out.

3.5.2 ^{21}N incident beam selection

A similar approach has been applied to the incident beam selection of ^{21}N. Initially, the correlation between Z and Y at F11 before the target was examined with a rough selection

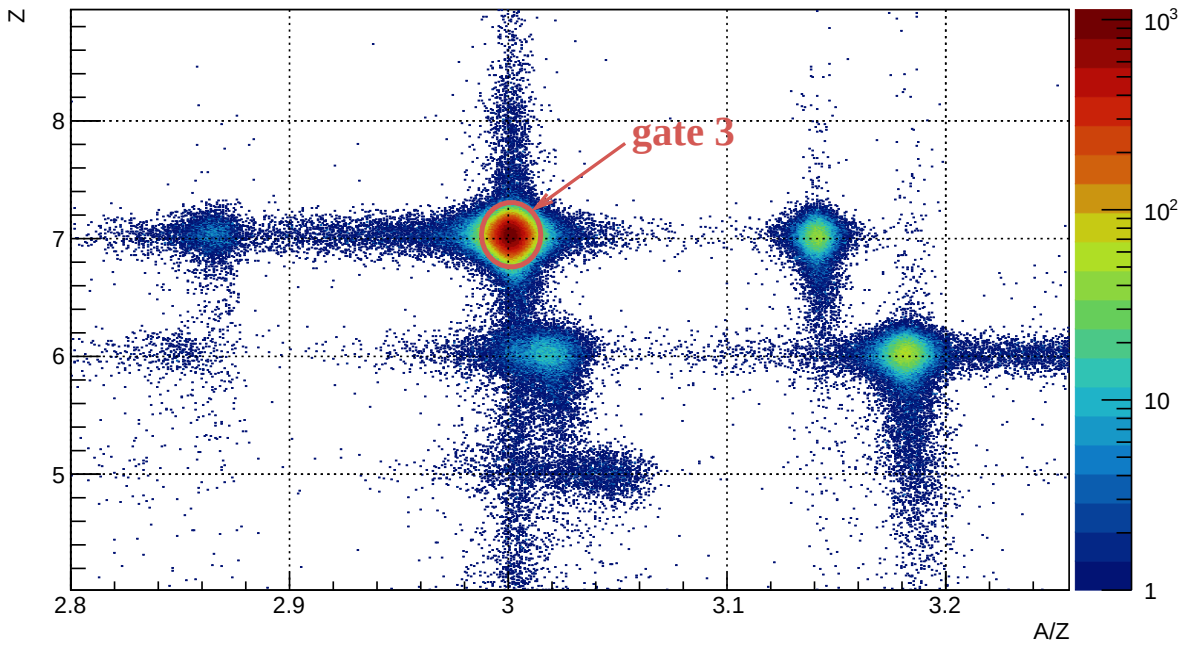

Figure 3.12: PID at F11 before target. The geometric cut (*gate 3*) represents the extended selection of ^{21}N.

of ^{21}N (*gate 3*) as shown in Fig. 3.12. Due to a more restricted selection of ^{21}N in the PID, the tail is notably shorter in nature (Fig. 3.13). However, the central part was still selected

(*gate 4*) since rejecting events inside the tail improved the resolution of the Z spectrum after the reaction target. Similar to the ^{23}N case, even with this tail rejection before the target, the correlation plot of Z after the reaction target vs. Y from MUSIC2 also shows

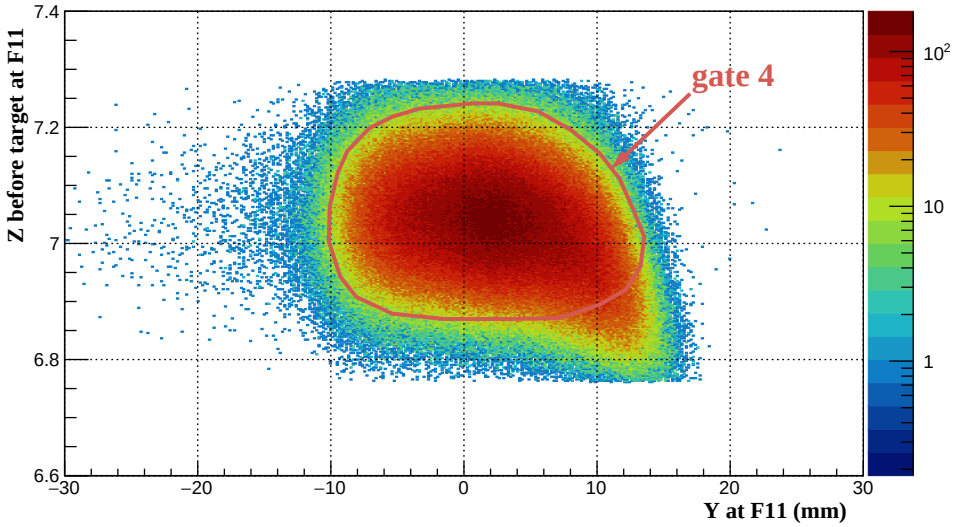

Figure 3.13: Correlation plot between Z before the target at F11 and the vertical position (Y) from MUSIC before the target at F11 with extended ^{21}N (*gate 3*) selection.

a tail-type correlation. However, restricting Y at F11 before the target doesn't provide a solution. Therefore, an investigation into the origin of these events was conducted by examining the correlation between after target Z and vertical position at F9 (Y9). As shown in Fig. 3.14, the imposition of a restriction on the Y9 position from -13.5 mm to 11.5 mm notably enhances the separation between $Z = 6$ and $Z = 7$ in the Z spectrum after the reaction target. Consistent with the approach applied to the ^{23}N data files, events with ADC overflow in the MUSIC detector positioned before the target at F11 have been excluded during the incident beam selection process, in addition to all the previously implemented selections.

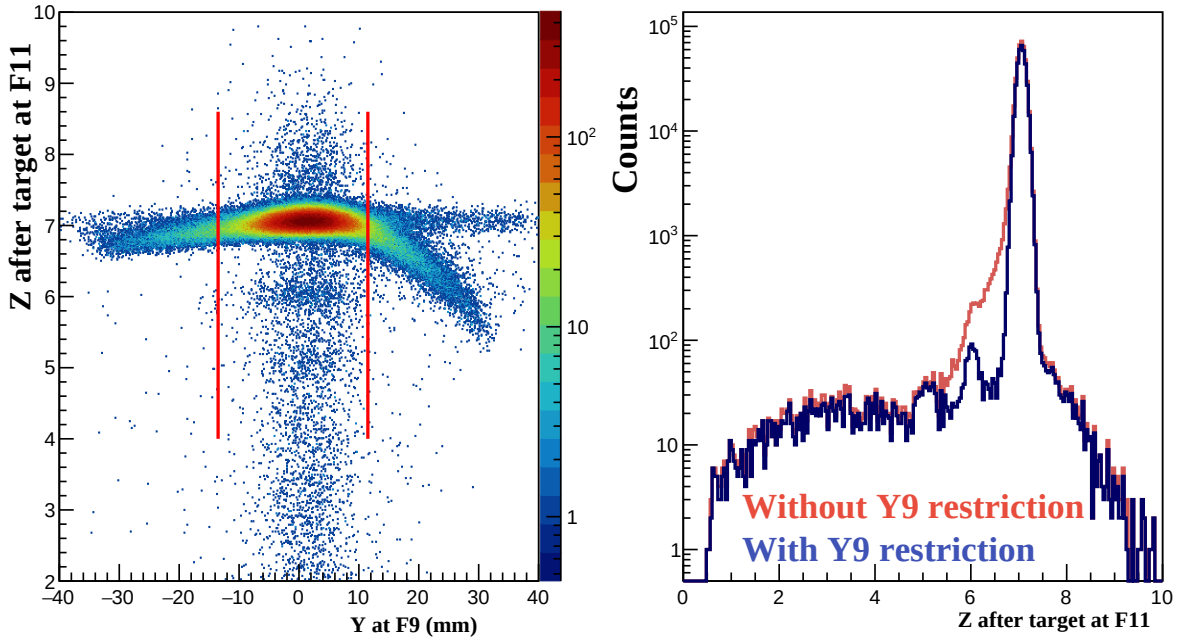

Figure 3.14: Left: Correlation plot between Z after the target at F11 and Y at F9 (mm) for ^{21}N with *gate 3* & *gate 4*. Right: The effect of the Y9 restriction ($-13.5 \leq Y9 \leq 11.5$) on the Z spectrum after the reaction target.

3.6 Z identification after the reaction target at F11

As discussed in Section 3.1, the Z spectrum after the reaction target has been obtained from the energy loss information in MUSIC 2 placed after the target at F11. However, from the individual spectrum of each of the 8 anodes of MUSIC2 positioned downstream from the target at F11, it has been observed that the 4th anode has presented issues. Hence, the 4th anode has been omitted while computing the geometric mean of the remaining anodes to obtain the Z spectrum after the reaction target.

3.6.1 Z after the reaction target for ^{23}N data

The Z spectrum after the reaction target is shown with final PID selection (Fig. 3.15), which consists of the graphical events restrictions mentioned before and the phase space selection discussed in later sections. The blue histogram represents the Z spectrum for

the target-in measurements, and the red histogram represents the target-out measurements, where the target-out spectrum is normalized to the target-in spectrum using the incident beam events.

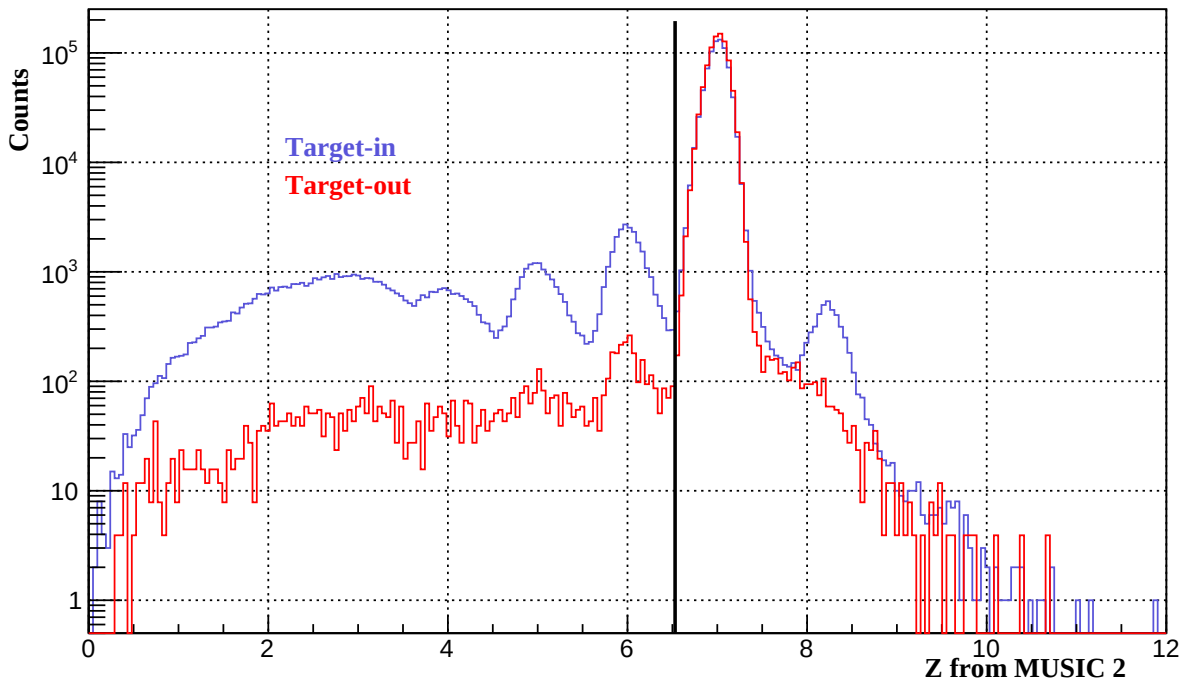

Figure 3.15: Z spectrum after the reaction target with ^{23}N incident beam selection - target-in (blue) and target-out (red) files. Z beyond the vertical black line will be considered for counting $N_{out \geq \text{Zincident}}$ in order to obtain the desired σ_{cc}.

However, as discussed previously, the charge-changing cross-section is based on the transmission technique. The transmission ratio (R_T) is determined from the ratio of proton-unreacted nuclei $N_{out \geq Z}$ and the incident particles N_{in}. The $N_{out \geq \text{Zincident}}$ are the particles with the proton number greater than or equal to the selected events of the incident beam N_{in}. In this case, it is $Z = 7$, as shown in Fig. 3.15. The spectrum shows three different particles apart from nitrogen ($Z = 7$); boron ($Z = 5$), carbon ($Z = 6$), and oxygen ($Z = 8$). $Z = 5, 6$ result from the incident nitrogen beam losing a proton, whereas $Z = 8$ is produced by picking up a proton from the reaction target. The production of the oxygen isotope with $Z = 8$ originates from the charge exchange where one proton

is added to the incident nucleus ^{23}N. These reactions do not involve interactions with the protons of the incident nitrogen isotope and will be considered in the N_{out} counting. Schematically, the Z beyond the vertical line shown in Fig. 3.15 will be considered to obtain the desired σ_{cc}. In order to accurately count the N_{out}, it's necessary to account for the influence of the contamination ($Z = 5, 6$) on the $Z = 7$ peak by subtracting it, while also adding the contribution of the $Z = 7$ tail to the $Z = 6$ peaks. Therefore, a precise fitting of both $Z = 6$ and $Z = 7$ is essential. A Gaussian fit for the $Z = 7$ peak appears insufficient when considering the complexity of the spectrum.

3.6.2 Z after the reaction target for ^{21}N data

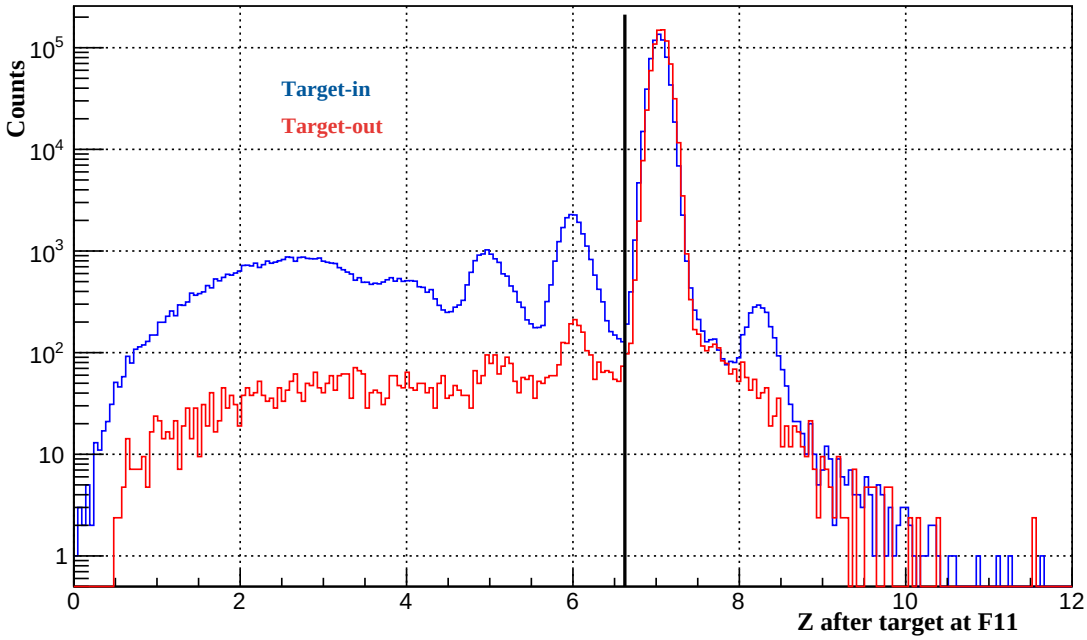

Figure 3.16: Z spectrum after the reaction target with ^{21}N incident beam selection - target-in (blue) and target-out (red) files. Z beyond the vertical black line will be considered for counting $N_{out \geq \text{Zincident}}$ in order to obtain the desired σ_{cc}.

Similar to the methodology employed for ^{23}N in 3.6.1, an analogous approach was employed for ^{21}N to get the Z after the reaction target. The Z spectrum after the re-

action target, in Fig. 3.16, incorporates the final PID selection involving graphical cuts as previously mentioned and phase space selection discussed in subsequent sections. The normalization of the target-out spectrum to the target-in spectrum is achieved by considering the ^{21}N incident beam events.

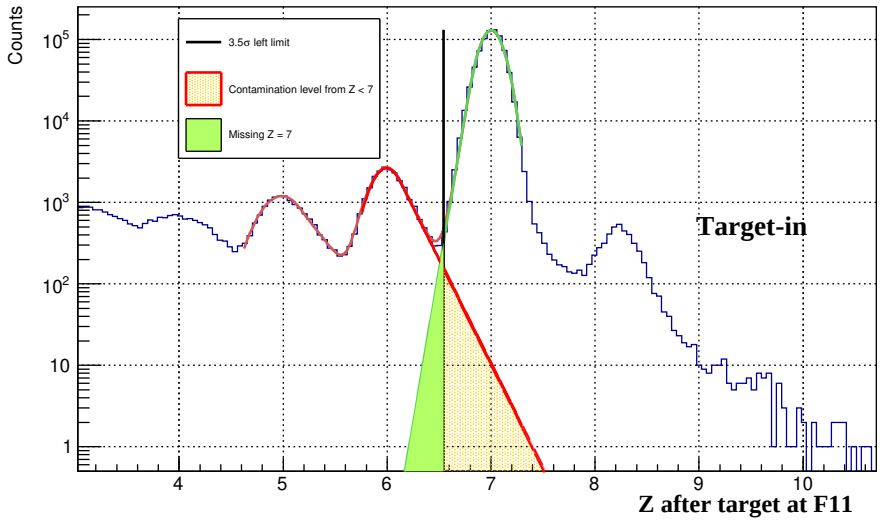

(a)

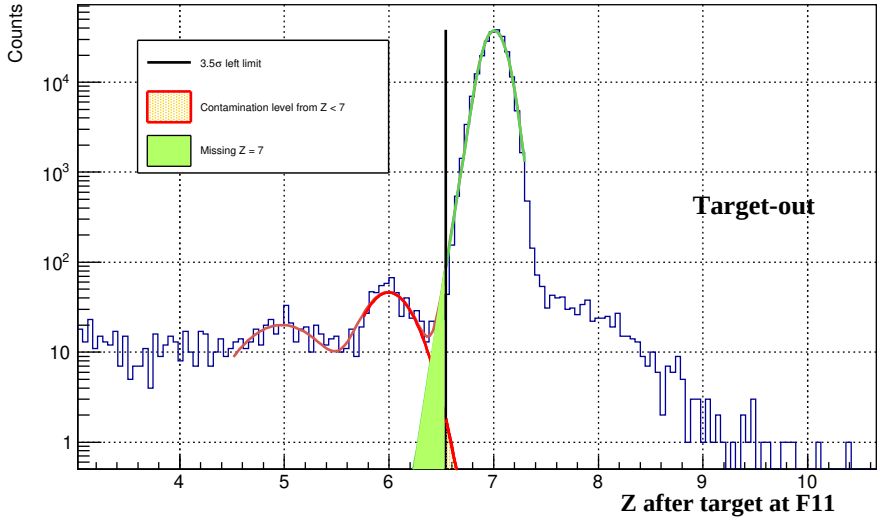

(b)

Figure 3.17: MUSIC2 (Z) spectrum for the (a) target-in and (b) target-out measurements of ^{23}N – fitted using the `GausExp` function.

3.7 Functions used for counting $N_{\text{out}\geq Z}$

The peaks at $Z = 5, 6, 7$ for both target-in and target-out measurements (Fig. 3.15, 3.16) exhibited skewness, indicating that a single Gaussian function is insufficient for accurate modeling. Consequently, a combination of two distinct functions, Gaussian and `GausExp` [74], was employed to establish lower limits (3.5σ) on the $Z = 7$ (peak) for the isotopes of interest, ^{21,23}N.

Fig. 3.17 illustrates the fitting of each of the $Z = 5, 6, 7$ peaks using a novel function named `GausExp`, which consists of four parameters: three from the Gaussian fit, and the fourth parameter, k, represents the exponential tail on the lower side of the Gaussian. The x, $\bar{x}$, and σ represent the counts, the mean, and the standard deviation obtained from the Gaussian fit, respectively, while k represents the number of standard deviations on the side of the tail where the Gaussian switches to an exponential, as given by the equation:

$$\begin{aligned} f(x;\bar{x};\sigma;k) &= e^{-\frac{1}{2}(\frac{x-\bar{x}}{\sigma})^2}, \quad \text{for } \frac{x-\bar{x}}{\sigma} \geq -k; \\ &= e^{\frac{k^2}{2}+k(\frac{x-\bar{x}}{\sigma})}, \quad \text{for } \frac{x-\bar{x}}{\sigma} < -k \end{aligned} \tag{3.17}$$

The 3.5σ region to the left of the $Z = 7$ peak is crucial for establishing a lower limit for counting $N_{\text{out}} \geq Z$ particles (7 in this case). The $Z = 5, 6$ peaks of boron and carbon isotope are fitted with the same `GausExp` to assess the total contamination levels within the set counting limits for $Z = 7$ particles. The yellow region indicates contamination from $Z < 7$ isotopes, while the green-filled region represents missing $Z = 7$ outside the 3.5σ counting region.

Counts from the green region ($Z = 7$) are added, and counts from the yellow region ($Z < 7$) are subtracted from $N_{\text{out}} \geq Z$ particle counts before determining the final cross-section. The estimated contamination from $Z < 7$ is approximately 6.8×10^{-4}

(1.1×10^{-5}) for ^{23}N target-in (target-out) measurements, as determined by the `GausExp` function. The $Z = 7$ counts missing from the lower limit of the 3.5σ region are around 4.9×10^{-4} for ^{23}N for both target-in and target-out measurements. For ^{21}N, the estimated contamination from $Z < 7$ is approximately 1.8×10^{-4} (2.7×10^{-4}) for target-in (target-out) measurements, as determined by the `GausExp` function (Fig. 3.18). The counts of $Z = 7$ missing from the lower limit of the 3.5σ region are around 4.9×10^{-4} (5×10^{-4}) for target-in (target-out) measurements.

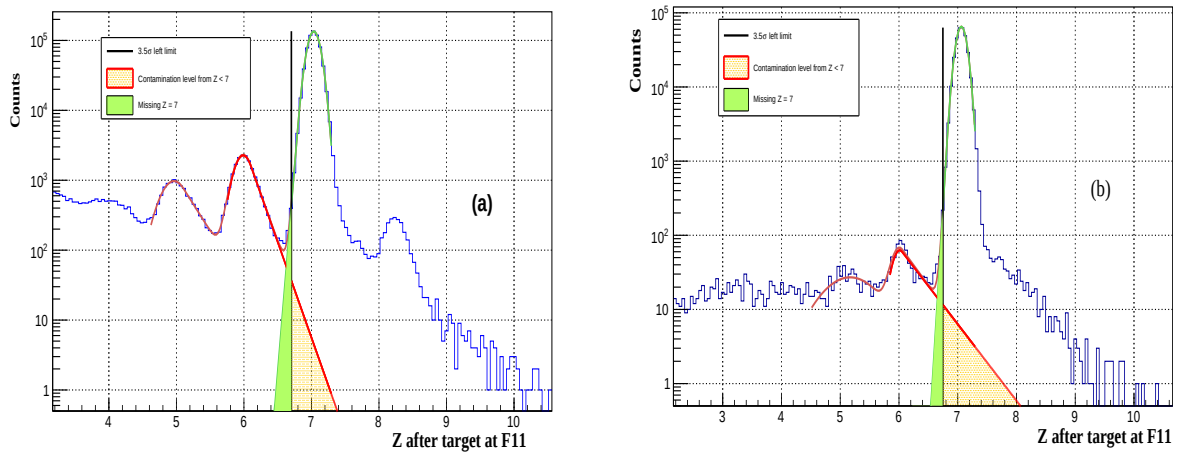

Figure 3.18: MUSIC2 (Z) spectrum for the (a) target-in and (b) target-out measurements of ^{21}N – fitted using the `GausExp` function.

The impact of contamination from $Z < 7$, the absence of $Z = 7$ counts, and the consistency in choosing a 3.5σ lower limit for $N_{\text{out}} \geq Z$ particles on the final σ_{cc} will be discussed in the following chapter.

3.8 Phase space restriction within a region of constant transmission

To mitigate losses of $N_{out \geq \text{Zincident}}$ events beyond the target resulting from large-angle scattering of particles outside the detector acceptance, it is necessary to limit the phase

space of incident beam events at the target location. This restriction is made based on a constant transmission ratio across different positions and angles at the reaction target location.

The horizontal position (X_T) and vertical position (Y_T) at the target location are determined based on the distance between the focus point at F11, determined by ion optics, and information regarding the horizontal and vertical positions at F11 (Eq. 3.18). This determination is facilitated by the double PPAC detectors located at F11. However, the horizontal angle (A_{11}) and vertical angle (B_{11}) at target location remain the same as they were at F11:

$$\begin{aligned} X_T &= X_{11} + 571 \cdot \tan\left(\frac{A_{11}}{1000.0}\right) \\ Y_T &= Y_{11} + 571 \cdot \tan\left(\frac{B_{11}}{1000.0}\right) \end{aligned} \tag{3.18}$$

here, 571 mm represents the distance between F11 and the target location, and the factor of 1000 is used for the conversion from milliradians to radians. Fig. 3.19 illustrates the spectrums of the horizontal position (X_T) and angle (A_{11}), and vertical position (Y_T) and angle (B_{11}) of the ^{23}N incident beam at the target location.

Particles not undergoing charge-changing reactions are represented using a transmission ratio, denoted as:

$$R_{T_{\text{in}}} = \frac{N_{\text{out}\geq Z}}{N_{\text{in}}} \tag{3.19}$$

where, N_{in} represents the count of incident particles, and $N_{\text{out}\geq Z}$ is the count of particles with Z values equal to or greater than those of the incident particles after interacting with the target. The same principle is applied to target out measurements ($R_{T_{\text{out}}} = \frac{N_{\text{out}\geq Z}}{N_{\text{in}}}$). These ratios quantify the transmission of incident and outgoing particles for non-target reactions. The selection of the constant region in R_T at each phase space is a critical step, involving an iterative process. The ultimate selection of the constant region in R_T

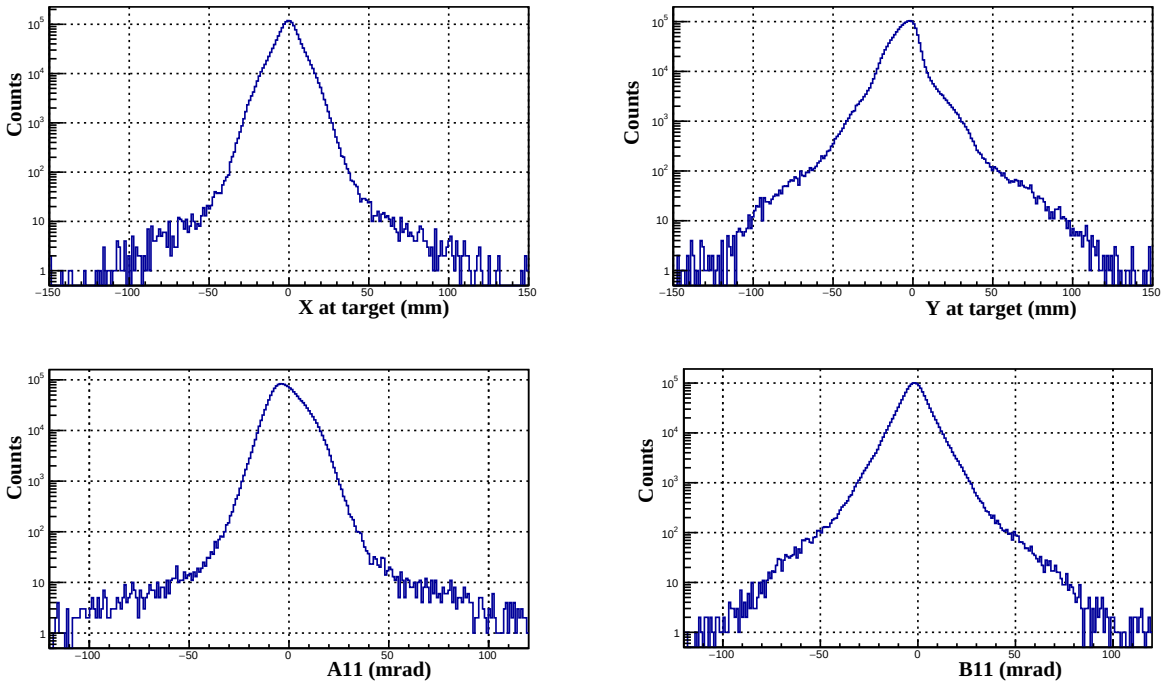

Figure 3.19: Horizontal position (X_T), angle (A_{11}), vertical position (Y_T), and angle (B_{11}) of the ^{23}N incident beam at the target location.

for each phase space is determined after examining all the phase spaces individually and subsequently iteratively reviewing all upstream phase spaces following the initial selections.

3.8.1 ^{23}N phase space selection

As discussed previously, the phase space selection is an iterative process. Initially, the constant transmission region was determined for the horizontal position at the target location (X_T). Subsequently, with the selected X_T phase space region, the vertical position at the target location (Y_T) was scrutinized. Following that, with restrictions on both X_T and Y_T, the horizontal angle (A_{11}) phase space was restricted. Finally, with restrictions on X_T, Y_T, and A_{11}, the vertical angle (B_{11}) phase space was examined. After a series of iterations, the phase space for each position and angle was examined with the phase space of the other variables restricted. The constant phase space from the final iteration

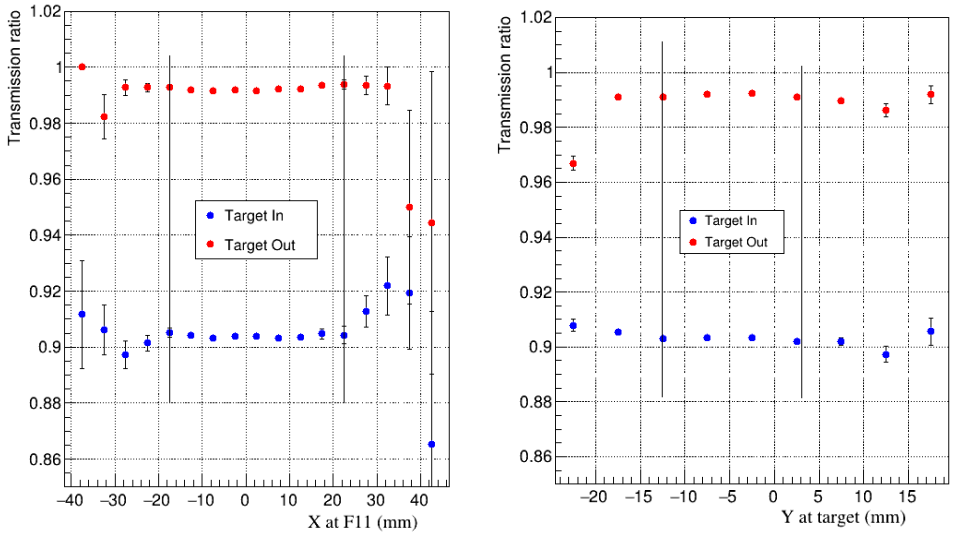

(a) **(b)**

Figure 3.20: Transmission ratio variation for different (a) X (mm) and (b) Y (mm) at the target location with ^{23}N incident beam selection. Vertical lines show the region of constant transmission.

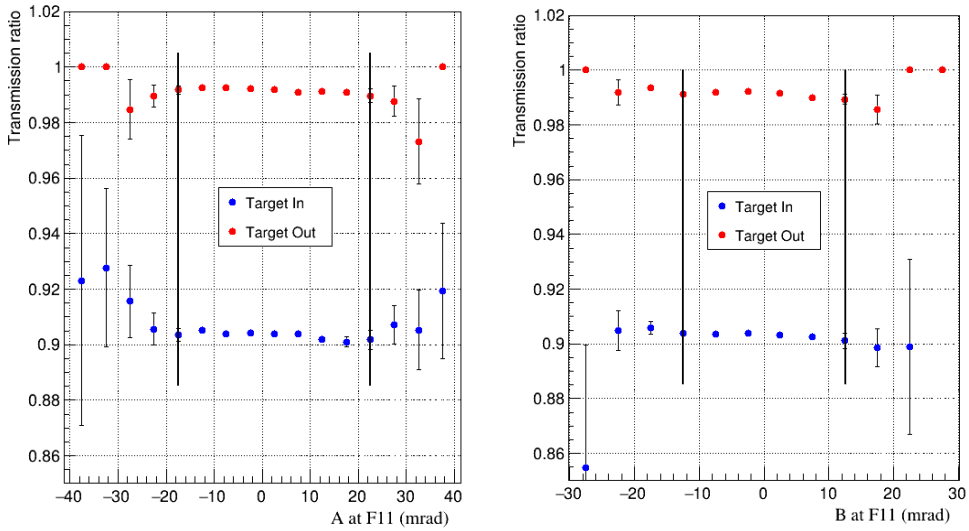

(a) **(b)**

Figure 3.21: Transmission ratio variation for different (a) A11 (mrad) and (b) B11 (mrad) at the target location with ^{23}N incident beam selection. Vertical lines show the region of constant transmission.

is shown in Fig. 3.20 for each of X_T, Y_T, A_{11}, and B_{11}, while the rest of the variables remain constant. R_T for the X and Y at the reaction target location, was determined

at 5 mm intervals for selected isotope of interest. The vertical bars represent statistical uncertainty in R_T. The methodology for determining statistical uncertainty in R_T will be elaborated in the final chapter. The transmission ratios $R_{T_{\text{out}}}$ (red points) and $R_{T_{\text{in}}}$ (blue points) for ^{23}N exhibit a constant trend from X = -17.5 mm to 22.5 mm and Y = -17.5 to 2.5 mm. The constant region of the transmission ratio, indicated by black vertical lines, serving as the selected region in both $R_{T_{\text{out}}}$ and $R_{T_{\text{in}}}$ to obtain σ_{cc}. Similarly, the horizontal angle (A11) and vertical angle (B11) have also been examined for a constant transmission region with the ^{23}N incident beam selection. Fig. 3.21 illustrates the selected phase space regions for A11 and B11, with vertical black lines representing the region of constant transmission. For A11 ranging from -17.5 mrad to 22.5 mrad and B11 from -12.5 mrad to 12.5 mrad, a constant trend is observed. This region has been selected for the phase space of incident ^{23}N beam selection.

It is also necessary to restrict the incident beam in momentum space to ensure that the events selected to compute the desired cross-section follow a specific trajectory and

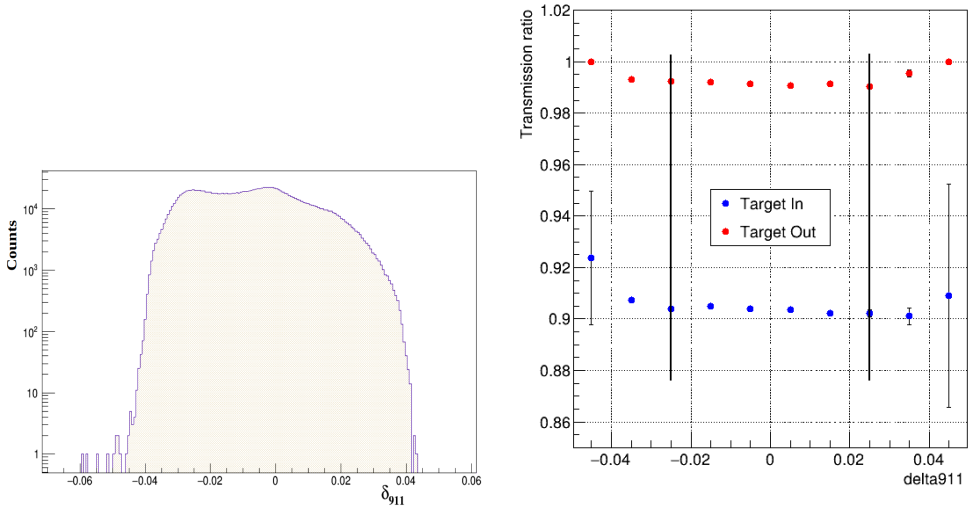

(a) **(b)**

Figure 3.22: (a)The momentum spread (δ_{911}) distribution and (b) Transmission ratio variation for different δ_{911} intervals for the ^{23}N incident beam.

have consistent momentum characteristics. Therefore, a constant transmission region

has been studied with the entire range of momentum spread (δ_{911}), computed from the deviation from the central trajectory from F9 to F11. Fig. 3.22 depicts the distribution of momentum spread with the ^{23}N incident beam selection and the constant transmission region of δ_{911}, obtained with the above restrictions in the phase space of X_T, Y_T, $A11$, and $B11$. A constant transmission region has been observed for $\delta_{911} = -0.025$ to 0.025 for the ^{23}N incident beam. With these phase restrictions, in conjunction with previous graphical cuts in the PID plot, the incident beam events (N_{in}) have been identified for both target-in and target-out measurements and will be utilized for the calculation of σ_{cc}.

3.8.2 ^{21}N phase space selection

Similar to the methodology applied for ^{23}N in 3.8.1, an iterative process was undertaken to determine the phase space restrictions for the ^{21}N incident beam selection. After in-

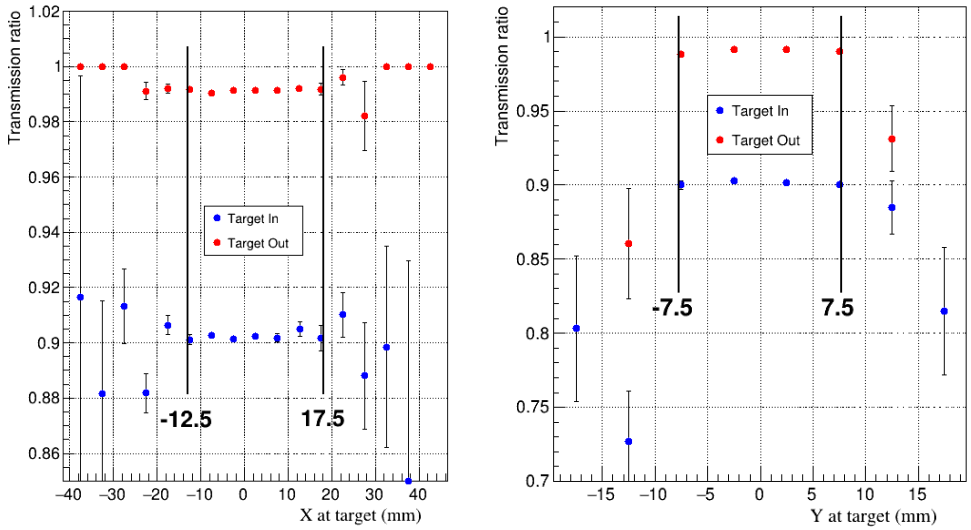

(a) **(b)**

Figure 3.23: Transmission ratio variation for different (a) X (mm) and (b) Y (mm) at the target location with ^{21}N incident beam selection. Vertical lines show the region of constant transmission.

dividual restrictions on each variable (X_T, Y_T, A_{11}, and B_{11}), a combined phase space

restriction analysis was carried out to select the phase space for a variable with phase space restrictions on all other variables obtained from the final iteration. Figures depicting the constant phase space for each variable from the final iteration are attached (Fig. 3.23, 3.24) with vertical lines denoting the constant region of the transmission ratio. Mo-

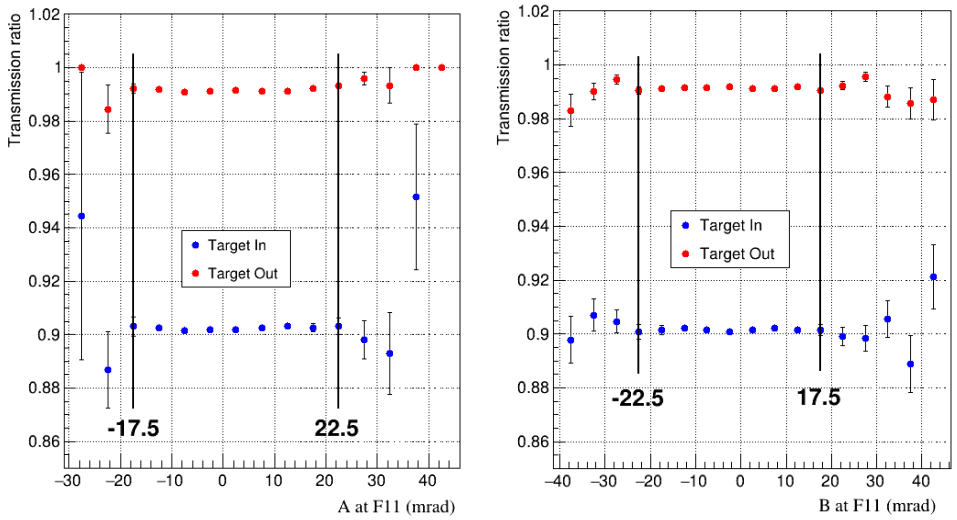

(a) **(b)**

Figure 3.24: Transmission ratio variation for different (a) A11 (mrad) and (b) B11 (mrad) at the target location with ^{21}N incident beam selection. Vertical lines show the region of constant transmission.

mentum space was also considered, and Fig. 3.25 displays the distribution of momentum spread (δ_{911}) with the ^{21}N incident beam and the constant transmission region of δ_{911}, obtained with the above restrictions in the phase space of X_T, Y_T, $A11$, and $B11$. For the final phase space selection, X_T ranges from -12.5 to 17.5 mm (Fig. 3.23a), Y_T ranges from -7.5 to 7.5 mm (Fig. 3.23b), A_{11} ranges from -17.5 to 22.5 mrad (Fig. 3.24a), B_{11} ranges from -22.5 to 17.5 mrad (Fig. 3.24b), and δ_{911} ranges from -0.0005 to 0.0055 (Fig. 3.25). The phase space restrictions, along with graphical cuts in the PID plot, were employed to identify incident beam events (N_{in}) in both target-in and target-out measurements. This identification laid the groundwork for the subsequent measurement of σ_{cc}, which is discussed in the following chapter.

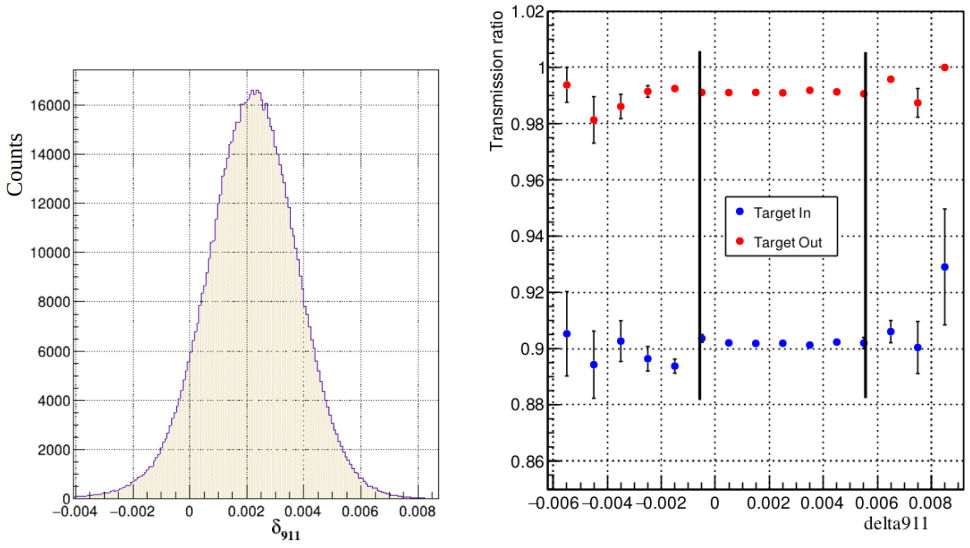

(a) **(b)**

Figure 3.25: (a)The momentum spread (δ_{911}) distribution and (b) Transmission ratio variation for different δ_{911} intervals for the ^{23}N incident beam.

Chapter 4

Results and discussion

4.1 Charge-changing cross section (σ_{cc})

The σ_{cc} is determined through the transmission technique outlined in Eq. 2.7, where $R_{T\text{in}}$ and $R_{T\text{out}}$ represent the transmission ratios of incident and outgoing particles with and without the reaction target, respectively. The variable t is the number of target atoms per cm^2 and is described by the equation:

$$t = d \times \frac{N_a}{M_u} \tag{4.1}$$

where $N_a = 6.022 \times 10^{23}$ is Avogadro's number, $M_u = 12.0107u$ is the molar mass of carbon, and $d = 2.5\,\text{g/cm}^2$ is the thickness of the carbon reaction target used during the experiment.

4.1.1 Measured σ_{cc} of nitrogen isotopes

The transmission ratios, denoted as $R_{T\text{in}}$ and $R_{T\text{out}}$, have been determined for neutron-rich nitrogen isotopes (^{21}N and ^{23}N). This involves the event-by-event counts for the selected incident beam integrating over the constant transmission region across various

beam phase space parameters such as horizontal position (X), vertical position (Y), and the horizontal angle (A) and vertical angle (B) at different focal planes, as detailed in the Section 3.5. The data corresponding to $R_{T\text{in}}$ and $R_{T\text{out}}$ for ^{21}N are depicted by the blue and red symbols, respectively, obtained when BigRIPS and ZDS were centered for

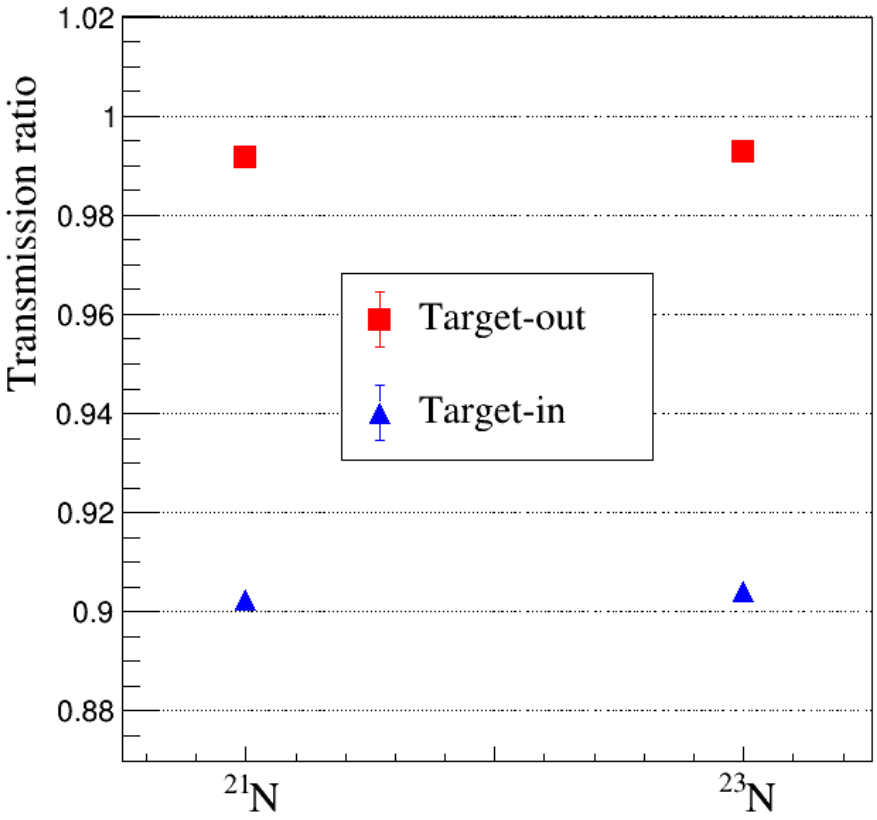

Figure 4.1: Transmission ratios for target-in & out set up with ^{21,23}N incident beams. The statistical uncertainties associated with these transmission ratio measurements are within the sizes of the symbols shown.

^{20}C. Similarly, the yellow and green symbols represent $R_{T\text{in}}$ and $R_{T\text{out}}$ for ^{23}N, acquired when the BigRIPS and ZDS was centered for ^{22}C. The uncertainties associated with these transmission ratio measurements are within the sizes of the symbols shown in Fig. 4.1. Fig. 4.2 displays the measured σ_{cc} obtained using the Eq. 2.7 & 4.1 for ^{21,23}N. The uncertainties shown in the measured σ_{cc} in Fig. 4.2 account for both statistical and

systematic uncertainties, as elaborated in the subsequent section.

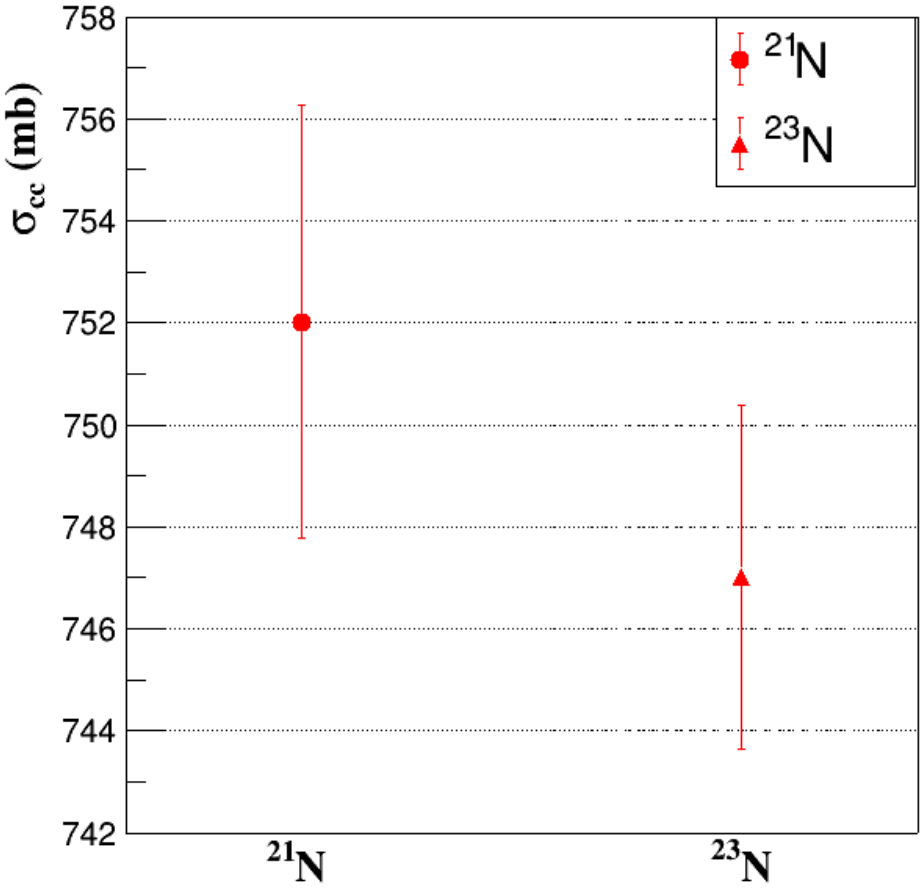

Figure 4.2: Measured charge-changing cross-section (σ_{cc}) of ^{21,23}N isotopes.

4.2 Uncertainty in the measured σ_{cc}

The uncertainty in σ_{cc} arises from statistical variations in the number $N_{\text{out}\geq Z}$ of events occurring after the target, the measurement of target thickness, and the selection region for counting $N_{\text{out}\geq Z}$ events. Both systematic and statistical uncertainties were determined for the σ_{cc} across each isotope. The number of incident particle events (N_{in}) selected for each isotope, as explained in Section 3.5, has no statistical uncertainty since these counts

result from the desired event-by-event selection of the secondary beam. There is no DAQ dead-time effect on σ_{cc} due to the event-by-event counting method used here. The systematic uncertainty arises from the measurement of the target thickness and from the estimation of contaminant contribution derived using fit parameters used to fit the Z spectrum after the target in both target-in and target-out measurements. The formula used for the statistical and systematic uncertainty will be explained in the following sections.

4.2.1 Statistical uncertainty in σ_{cc}

The primary source of error in the experiment is the statistical uncertainty, which significantly impacts the measured charge-changing cross-section (σ_{cc}). The standard deviation of σ_{cc} due to statistical uncertainty is determined by the equation:

$$\Delta\sigma_{cc} = \sqrt{\left(\frac{\partial\sigma_{cc}}{\partial R_{T\text{in}}}\right)^2 \Delta R_{T\text{in}}^2 + \left(\frac{\partial\sigma_{cc}}{\partial R_{T\text{out}}}\right)^2 \Delta R_{T\text{out}}^2} \tag{4.2}$$

Here, $\Delta R_{T\text{in}}$ and $\Delta R_{T\text{out}}$ are the standard deviations of transmission ratios $R_{T\text{in}}$ and $R_{T\text{out}}$ respectively. The transmission ratio (R_T) represents the ratio of particles after and before the reaction target, incorporating statistical considerations. The partial derivatives of σ_{cc} with respect to $R_{T\text{in}}$ and $R_{T\text{out}}$ are given by:

$$\frac{\partial\sigma_{\text{cc}}}{\partial R_{T\text{in}}} = -\frac{1}{t}\frac{1}{R_{T\text{in}}} \tag{4.3}$$

$$\frac{\partial\sigma_{\text{cc}}}{\partial R_{T\text{out}}} = \frac{1}{t}\frac{1}{R_{T\text{out}}} \tag{4.4}$$

By substituting these derivatives into Equation (4.2), the statistical uncertainty $\Delta\sigma_{cc}^{stat}$ can be expressed as:

$$\Delta\sigma_{cc}^{stat} = \sqrt{\frac{1}{t^2}\left[\left(\frac{\Delta R_{T\text{in}}}{R_{T\text{in}}}\right)^2 + \left(\frac{\Delta R_{T\text{out}}}{R_{T\text{out}}}\right)^2\right]} \tag{4.5}$$

The uncertainty in counts from the secondary beam selection is considered, and the binomial distribution variance (i.e. $Var(X) = n \cdot p \cdot [1-p]$) is used to calculate $\Delta R_{T\text{in}}$ and $\Delta R_{T\text{out}}$:

$$\left(\frac{\Delta R_{T\text{in}}}{R_{T\text{in}}}\right)^2 = \frac{1 - R_{T\text{in}}}{N_{T\text{in}} R_{T\text{in}}} \tag{4.6}$$

$$\left(\frac{\Delta R_{T\text{out}}}{R_{T\text{out}}}\right)^2 = \frac{1 - R_{T\text{out}}}{N_{T\text{out}} R_{T\text{out}}} \tag{4.7}$$

The statistical uncertainty of the cross-section ($\Delta\sigma_{cc}^{stat}$) is then given by:

$$(\Delta\sigma_{cc}^{stat})^2 = \frac{1}{t^2}\left(\frac{1 - R_{T\text{in}}}{N_{T\text{in}} R_{T\text{in}}} + \frac{1 - R_{T\text{out}}}{N_{T\text{out}} R_{T\text{out}}}\right) \tag{4.8}$$

4.2.2 Uncertainty in σ_{cc} due to target thickness ($\sigma_{cc}^{\Delta t}$)

The measurement of the target thickness introduces an additional uncertainty that must be taken into account. The standard deviation of the measured charge-changing cross-section for systematic uncertainty is expressed by the equation:

$$\Delta\sigma_{cc} = \sqrt{\left(\frac{\partial\sigma_{cc}}{\partial t}\right)^2 \Delta t^2} \tag{4.9}$$

Here, Δt represents the standard deviation in the measurement of the target thickness, which serves as the systematic uncertainty in the measured σ_{cc}. The partial derivative is given by:

$$\frac{\partial\sigma_{\text{cc}}}{\partial t} = \frac{1}{t^2} \ln \frac{R_{T\text{out}}}{R_{T\text{in}}} \tag{4.10}$$

Substituting Equation (4.10) into Equation (4.9) yields:

$$\Delta\sigma_{cc} = \sqrt{\left(\frac{1}{t}\ln\frac{R_{T\text{out}}}{R_{T\text{in}}}\right)^2\left(\frac{\Delta t}{t}\right)^2} \tag{4.11}$$

In Equation (4.11), the term Δt denotes the standard deviation in the measurement of the target thickness. The uncertainty in the measured cross-section due to unceratinty in target thickness, $\Delta\sigma_{cc}^{\Delta t}$, is then expressed as:

$$\left(\frac{\Delta\sigma_{cc}^{\Delta t}}{\sigma_{cc}}\right)^2 = \left(\frac{\Delta t}{t}\right)^2 \tag{4.12}$$

The C reaction target (2.5 g/cm^2) at F11 had a measured thickness of 13.704 mm with a standard deviation of $\Delta t = 0.014$ mm. The standard deviation found for the target thickness is substituted into Eq. (4.12) to determine Δt. The systematic uncertainties for different isotopes are presented in the table 4.2 of charge-changing cross-sections.

The expression for the combined uncertainty from statistical unceratinty and due to target thickness ($\Delta\sigma_{cc}^{stat+\Delta t}$) is given by:

$$\Delta\sigma_{cc}^{stat+\Delta t} = \sqrt{\left(\frac{\partial\sigma_{\text{cc}}}{\partial R_{T\text{in}}}\right)^2\Delta R_{T\text{in}}^2 + \left(\frac{\partial\sigma_{\text{cc}}}{\partial R_{T\text{out}}}\right)^2\Delta R_{T\text{out}}^2 + \left(\frac{\partial\sigma_{\text{cc}}}{\partial t}\right)^2\Delta t^2} \tag{4.13}$$

The partial derivatives of N_t, $R_{T\text{in}}$, and $R_{T\text{out}}$ given in the previous sections are used to obtain the combined $\Delta\sigma_{\text{cc}}$:

$$\left(\frac{\Delta\sigma_{cc}^{stat+\Delta t}}{\sigma_{cc}}\right) = \sqrt{\left[\left(\frac{\Delta R_{T\text{in}}}{R_{T\text{in}}}\right)^2 + \left(\frac{\Delta R_{T\text{out}}}{R_{T\text{out}}}\right)^2\right]\left(\ln\frac{R_{T\text{out}}}{R_{T\text{in}}}\right)^{-2} + \left(\frac{\Delta t}{t}\right)^2} \tag{4.14}$$

Substituting the variances of $\Delta R_{T\text{out}}$ and $\Delta R_{T\text{in}}$ into Equation (4.14), the combined uncertainty is given by:

$$\left(\frac{\Delta\sigma_{cc}^{stat+\Delta t}}{\sigma_{cc}}\right)^2 = \left[\frac{1-R_{Tin}}{N_{Tin}R_{Tin}} + \frac{1-R_{Tout}}{N_{Tout}R_{Tout}}\right]\left(\frac{1}{\sigma_{cc}\cdot t}\right)^2 + \left(\frac{\Delta t}{t}\right)^2 \tag{4.15}$$

4.2.3 Uncertainty from the $N_{out<Z}$ in the $N_{out\geq Z}$ events

The analysis involved counting $N_{out\geq Z}$ events after the target at F11 by establishing a lower limit in the 3.5σ region around the mean position of the Z of interest. In evaluating the consistency of this 3.5σ selection limit, it was noted that for both ^{21}N and ^{23}N, the values of σ_{cc} are consistent within the uncertainties across lower limit selections of 3σ, 3.3σ, and 3.6σ (Fig. 4.3). Therefore, for subsequent discussions, the 3.5σ lower selection

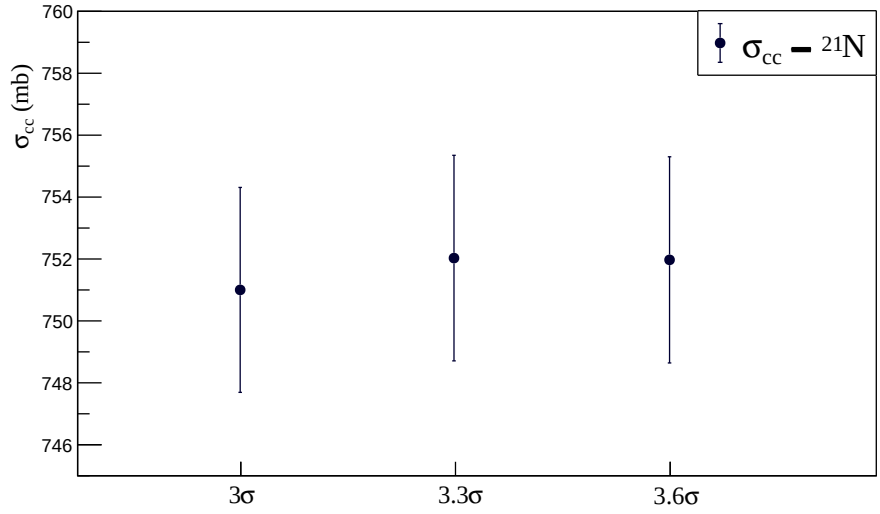

Figure 4.3: Comparison of σ_{cc} values for ^{21}N with various lower limit selections. The σ_{cc} values align consistently with lower limit selections at 3σ, 3.3σ, and 3.6σ for ^{21}N. Similar consistency has also been observed for ^{23}N across different lower limit selections.

limit has been opted for. As discussed in the previous chapter, the selection of these $N_{out\geq Z}$ events includes some contamination from lower Z events and missing events of the desired nitrogen isotope that extend to the lower Z direction below the 3.5σ selection boundary. The contribution from lower Z contaminants (Orange region in Fig. 3.17; Z_{cont}) introduces uncertainty in determining σ_{cc}. As depicted in Fig. 3.17, the peak of interest ($Z = 7$) has non-negligible counts, as shown by the green shaded region

($Z_{N\text{missing}}$) outside the lower limit set for counting $N_{\text{out}\geq Z}$ particles. Consequently, these counts should be added to the $N_{\text{out}\geq Z}$ counts.

The absolute value of σ_{cc} is determined using the transmission ratios, $R_{T\text{ in}} = N_{\text{out}\geq Z}/N_{\text{in}}$, as discussed in Section 4.1. The transmission ratio equation is adjusted to account for contamination from $Z < 7$, and the inclusion of the missing $Z = 7$ ($Z_{N\text{missing}}$) events within the selection boundary in the counting of $N_{\text{out}\geq Z}$:

$$N^{*}_{\text{out}\geq Z} = N_{\text{out}\geq Z} + (Z_{N\text{missing}} - Z_{\text{cont}})$$

The modified equation for the transmission ratio, $R^{*}_{\text{in}} = N^{*}_{\text{out}\geq Z}/N_{\text{in}}$, was used to determine the transmission ratios for both target in and out measurements. The fitting of both the target-in and target-out spectra with the `GausExp` function, as discussed in Section 3.7, involves 3-4 parameters for each peak, depending on the skewness. Each parameter in the best fit curve has its uncertainity. The individual unceratinty in each parameter has been considered by adding and subtracting to the mean value of the parameter, while keeping all other parameters constant to get σ_{cc}. A spread of 749.2 to 754.2 mb in σ_{cc} has been observed for ^{21}N, while a range of 746.4 to 748.3 mb in σ_{cc} has been observed for ^{23}N due to the lower and higher limits in all possible combinations of the parameters. Consequently, the uncertainty in the measured σ_{cc} due to these fit parameters ($\Delta\sigma_{cc}^{fitpars}$) is considered to be half of this spread in σ_{cc}. This results in an $\Delta\sigma_{cc}^{fitpars}$ of $\pm$2.5 mb for ^{21}N and $\pm$0.95 mb for ^{23}N.

However, even with this conservative approach, the uncertainty from fit parameters is lower than the statistical uncertainty of the measured σ_{cc}. As a result, the uncertainty from fit parameters doesn't significantly impact the total uncertainty in the measured σ_{cc}.

4.2.4 Total uncertainty of the measured σ_{cc}

The sources of uncertainty included statistical variations in the number of events ($N_{\text{out}\geq Z}$), target thickness measurement, and the selection region for counting $N_{\text{out}\geq Z}$ events. The total uncertainty, combining these factors, is determined to be ± 4.23 mb for ^{21}N and ± 3.37 mb for ^{23}N (Table 4.2). The central values and their corresponding uncertainties are depicted in Fig. 4.2.

4.3 Impact of VETO scintillator on σ_{cc}

As discussed in the Section 2.6.4, during the experiment the veto scintillator was placed in front of the carbon target at F11 to remove any spurious events due to multi-hit from scattering of low Z particles upstream of the target during offline analysis. For both ^{21,23}N incident beams, excluding events at higher QDC channel numbers – corresponding to events detected in the veto scintillators – the resulting charge-changing cross-sections were examined. The measured σ_{cc} values for both ^{21}N and ^{23}N, with and without events detected in the veto scintillator, are presented in Table 4.2. Uncertainties were determined following the same methodology discussed earlier. The σ_{cc} values for both isotopes showed agreement within uncertainties in both cases. Given this consistency, no additional rejection was implemented based on the VETO scintillator during the incident beam selection.

4.4 Determination of beam energies before the reaction target at F11

In the Glauber model framework, the finite-range profile function $\Gamma_{NN}(b)$ for the nucleon-nucleon (NN) scattering involves several parameters, α_{NN}, β_{NN}, and σ_{NN}^{total}, as discussed in Eq. 1.13. The values of these parameters in the profile function are energy dependent.

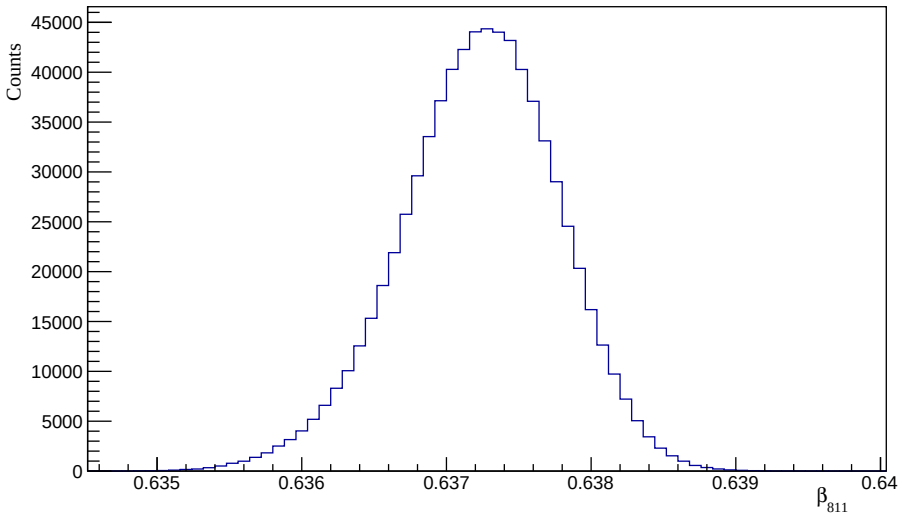

Figure 4.4: Velocity (β_{811}) profile for the ^{21}N particles measured using plastic scintillators located at F11 (PS11) and F8.

Thus, it is crucial to know the energy of the incident beams to extract the proton radius from the measured charge-changing cross sections. The determination of beam energy involves measuring the velocities (β_{811}) of incident particles using plastic scintillators located at F11 (PS11) and F8. For ^{21}N, the mean value of the β spectrum (Fig. 4.4) is measured at 0.64, corresponding to an energy of 277A MeV. Using the LISE++ tool [75], which accurately simulates the beam propagation and ion optics through BigRIPS and ZDS, the energy lost by the incident particle while passing through the various materials between the plastic detector (PS11) and the reaction target at F11 is quantified. The beam energy for ^{21}N before reaching the target is determined to be 264A MeV, and after passing through the target, it is 244A MeV. Therefore, an average of these two energies

Table 4.1: Beam energy for different isotopes at different positions at F11.

Isotopes	β_{811}	Beam energy (E/A in MeV)			
		Before PS11	Before the target	After the target	At mid-target
^{21}N	0.64	277	264	244	254
^{23}N	0.62	253	241	221.5	231

is adopted for the energy at the mid-target region. Similarly, for ^{23}N, following same method, the calculated β_{811} spectrum has a mean value of 0.62, corresponding to 253A MeV. The beam energy for ^{23}N before and after passing through the target is 241 and 221.5 A MeV, respectively, resulting in an energy of 231A MeV at the mid-target region. A summary of the beam energies at different positions is provided in Table 4.1.

4.5 Summary: σ_{cc} and uncertainties of different isotopes

The charge-changing cross-sections (σ_{cc}) of ^{21}N and ^{23}N isotopes were investigated using the BigRIPS and ZeroDegree Spectrometer (ZDS) setup. Transmission ratios ($R_{T\text{in}}$ and $R_{T\text{out}}$) were measured for incident beams ^{21}N and ^{23}N. The σ_{cc} values were determined, considering uncertainties from statistical variations in event counts, target thickness measurement, and the selection region for counting events after the target. The impact of the veto scintillator on σ_{cc} was assessed, and found to have no effect on the charge-changing cross sections. Table 4.2 provides a summary of the results and uncertainties, offering a comprehensive overview of charge-changing cross-section measurements for ^{21}N and ^{23}N isotopes.

Table 4.2: Charge-changing cross-sections (σ_{cc}) with uncertainties for ^{21,23}N.

Isotopes	Without Veto rejection					With Veto rejection					Energy at mid target
	σ_{cc}	$\Delta\sigma_{cc}^{stat.}$	$\Delta\sigma_{cc}^{syst.}$		$\Delta\sigma_{cc}^{total}$	σ_{cc}	$\Delta\sigma_{cc}^{stat.}$	$\Delta\sigma_{cc}^{syst.}$		$\Delta\sigma_{cc}^{total}$	
			$\Delta\sigma_{cc}^{fit\ pars}$	$\Delta\sigma_{cc}^{\Delta t}$				$\Delta\sigma_{cc}^{fit\ pars}$	$\Delta\sigma_{cc}^{\Delta t}$		
	(mb)										(MeV/u)
^{21}**N**	752	3.32	2.5	0.77	4	754	3.34	1.75	0.77	4	$\sim$ 254
^{23}**N**	747	3.14	0.95	0.76	3	744	3.24	0.8	0.76	3	$\sim$ 231

4.6 Discussion of results

The measured σ_{cc} values for ^{21}N and ^{23}N were 752 ± 4 mb (at $\sim 254A$ MeV) and 747 ± 3 mb (at $\sim 231A$ MeV) respectively. The determined σ_{cc} for ^{23}N was found to be comparable to that of ^{21}N within uncertainties.

As discussed in Section 1.2, S. Bagchi et al. [34] reported that the σ_{cc} on a carbon target at approximately $900A$ MeV for ^{21}N was 857 ± 7 mb, translating into a proton radius of $2.49(3)$ fm for ^{21}N. However, the matter radius obtained for ^{21}N is $2.78(2)$ fm. On the other hand, the matter radius of ^{23}N is reported to be 3.41 ± 0.23 fm, determined from interaction cross-section measurement [35]. The similar σ_{cc} for both nuclei (Fig. 4.5), despite the significantly larger matter radius of ^{23}N, suggest the possible existence of a two-neutron halo-type structure in ^{23}N. The decrease (within uncertainties) in the proton radius (R_p) from ^{17}N to ^{21}N (Fig. 1.5) with the filling of the $1d_{5/2}$ orbital reflects a strong attractive interaction between the proton in $1p_{1/2}$ ($l - \frac{1}{2}$) and the neutrons in $1d_{5/2}$ ($l + \frac{1}{2}$), leading to the emergence of a shell gap at $N = 14$ and a reduction in deformation. Ref. [34] also reports that the σ_{cc} for ^{22}N at around $900A$ MeV was 869 ± 7 mb, translating into a proton radius of $2.53(3)$ fm for ^{22}N. This observed increase in proton radius for ^{22}N, within the uncertainty, results from its extended neutron density for the valence neutron in the $2s_{1/2}$ orbital with a closed-shell core of ^{21}N. The motion of the center-of-mass (c.m.) of ^{22}N is therefore different from that of the core, causing the c.m motion smearing of the core density and hence an increased proton radius.

For ^{23}N, the neutrons ($N = 16$) in the most stable configuration fill the $2s_{1/2}$ orbital, and protons fill the $1p_{1/2}$ orbital. The measured σ_{cc} values for ^{21}N and ^{23}N agree within uncertainties (Fig. 4.5), and a previous study by Ref. [34] reports a higher σ_{cc} for ^{22}N compared to ^{21}N. This trend in the σ_{cc}, moving from ^{21}N to ^{23}N, with an increase in σ_{cc} for ^{22}N ($N = 15$), followed by a decrease in σ_{cc} for ^{23}N, signals the presence of a shell closure at $N = 16$. The shell closure at $N = 16$ is attributed to the absence of attractive monopole interaction between $n(1d_{3/2})$ neutrons and $p(1d_{5/2})$ protons, which are vacant

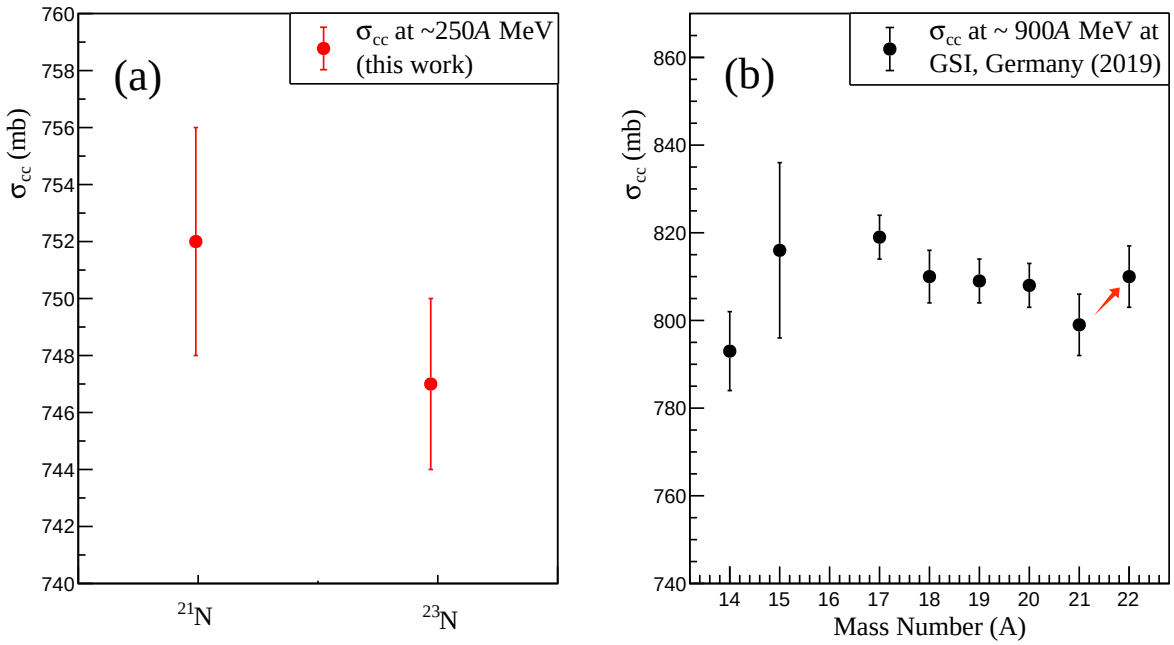

Figure 4.5: (a): Measured σ_{cc} for ^{21}N and ^{23}N from this work at $\sim$250A MeV.
(b): Measured σ_{cc} for the nitrogen isotopes at $\sim$900A MeV taken from Ref. [34]. The arrow indicates the observed increase in measured σ_{cc} (hence, in proton radius) for ^{22}N.

for ^{23}N. However, in stable nuclei, the shell gap at $N = 16$ disappears due to the nearly complete filling of the $p(1d_{5/2})$ shell.

The two-neutron separation energy (S_{2n}) for ^{23}N is 4.7 MeV, higher than its single-neutron separation energy (3.12 MeV) and the single-neutron separation energy of ^{22}N (1.28 MeV) [36, 37]. As explained in Eq. 1.4, the neutron density distribution is highly sensitive to the wave function of the valence neutron and its separation energy. A higher two-neutron separation energy in ^{23}N indicates a steeper density distribution tail (κ), posing a challenge to the halo formation in ^{23}N. This larger two-neutron separation energy in ^{23}N demonstrates strong binding of the valence neutrons in $n(2s_{1/2})$ and supports the presence of a shell closure at $N = 16$. The similar measurement of σ_{cc} (hence, proton radius) for both ^{21}N and ^{23}N suggests that the center-of-mass of the two valence neutrons in $n(2s_{1/2})$ of ^{23}N is not significantly spatially separated from that of the core.

The extracted proton radius from the measured σ_{cc} of ^{23}N, combined with its matter

radius, will contribute to determining the neutron radius and, consequently, the neutron skin thickness. This information will provide a comprehensive picture of the structure of this nitrogen nucleus at the drip-line. However, the current observations challenge the previously obtained large matter radius of ^{23}N, which had high uncertainty [35], and demand further precise measurements of this drip-line nitrogen isotope.

4.7 Future work

The measured charge-changing cross sections (σ_{cc}) for ^{21}N and ^{23}N isotopes provide crucial insights into their exotic neutron halo and neutron skin structures and the evolution of nuclear shells. The presented data also contribute significant evidence related to the potential origin of observed new shell gaps in neutron-rich nitrogen isotopes. The next goal will be the extraction of proton radii (R_p) from the measured σ_{cc} using the finite range Glauber model. The proton radius extracted from the measured σ_{cc} of ^{21}N at a beam energy different from that reported in Ref. [34] will be used as a comparison point with its radius derived from the previous study at GSI. This comparison will facilitate an assessment of the necessity for a scaling factor for the measured σ_{cc} in the intermediate energy range.

The extracted proton radii, in conjunction with the known matter radii (R_m), will enable the determination of the root mean square neutron radii (R_n) as described in Eq. 1.1. With the obtained information on neutron (R_n) and proton (R_p) radii, the neutron skin thickness (ΔR) will be determined through ($R_n - R_p$). The measurement of neutron skin thickness for ^{21,23}N isotopes near the drip line will significantly contribute to enhancing our understanding of their nuclear structure. Furthermore, the measured charge-changing cross section (σ_{cc}) in this experiment provides ground for further development of the state-of-the-art *ab initio* nuclear theories and the interactions utilized in various calculations.

Bibliography

[1] H. Geiger. On the Scattering of the α - Particles by Matter. *Proceedings of the Royal Society of London. Series A, Containing Papers of a Mathematical and Physical Character*, 81(546):174–177, 1908.

[2] E. Rutherford. LVII. The structure of the atom . *The London, Edinburgh, and Dublin Philosophical Magazine and Journal of Science*, 27(159):488–498, 1914.

[3] J. Chadwick. The existence of a neutron. *Proceedings of the Royal Society of London. Series A, Containing Papers of a Mathematical and Physical Character*, 136(830):692–708, 1932.

[4] Hideki Y. On the Interaction of Elementary Particles. I. *Proceedings of the Physico-Mathematical Society of Japan. 3rd Series*, 17:48–57, 1935.

[5] C. M. G. Lattes et al. Processes Involving Charged Mesons. *Nature*, 159:694–697, 1947.

[6] S. Kaur. *Determination of Proton Radii of Neutron-Rich Oxygen Isotopes from Charge-Changing Cross Section Measurements*. PhD thesis, 2018.

[7] K. S. Krane et al. *Introductory nuclear physics*. Wiley New York, New York, 1988.

[8] Maria G. Mayer. On Closed Shells in Nuclei. II. *Phys. Rev.*, 75:1969–1970, Jun 1949.

[9] Maria G. Mayer. Nuclear Configurations in the Spin-Orbit Coupling Model. I. Empirical Evidence. *Phys. Rev.*, 78:16–21, Apr 1950.

[10] O. Haxel et al. On the Magic Numbers in Nuclear Structure. *Phys. Rev.*, 75:1766–1766, Jun 1949.

[11] T. Otsuka. *Shell Structure of Exotic Nuclei*, pages 1–25. Springer Berlin Heidelberg, Berlin, Heidelberg, 2009.

[12] I. Tanihata. Nuclear physics using unstable nuclear beams. *Hyperfine Interactions*, 21(1):251–264, Jan 1985.

[13] I. Tanihata et al. Measurements of interaction cross sections and radii of He isotopes. *Physics Letters B*, 160(6):380–384, 1985.

[14] R. Kanungo. A new view of nuclear shells. *Physica Scripta*, 2013(T152):014002, jan 2013.

[15] SG. Zhou. Structure of Exotic Nuclei: A Theoretical Review, 2017.

[16] T. Aumann et al. The electric dipole response of exotic nuclei. *Physica Scripta*, 2013(T152):014012, Jan 2013.

[17] I. Tanihata et al. Halo and skin nuclei. *Comptes Rendus Physique*, 4(4):437–449, 2003.

[18] I. Tanihata. Neutron halo nuclei. *Journal of Physics G: Nuclear and Particle Physics*, 22(2):157, feb 1996.

[19] A.S. Jensen et al. Towards necessary and sufficient conditions for halo occurrence. *Physics Letters B*, 480(1):39–44, 2000.

[20] I. Angeli et al. N and Z dependence of nuclear charge radii. *Journal of Physics G: Nuclear and Particle Physics*, 36(8):085102, jun 2009.

[21] A. Ozawa et al. New magic number, $N = 16$, near the neutron drip line. *Phys. Rev. Lett.*, 84:5493–5495, Jun 2000.

[22] T. Otsuka et al. Evolution of nuclear shells due to the tensor force. *Phys. Rev. Lett.*, 95:232502, Nov 2005.

[23] S. Kaur et al. Proton Distribution Radii of $^{16-24}$O: Signatures of New Shell Closures and Neutron Skin. *Phys. Rev. Lett.*, 129:142502, Sep 2022.

[24] I. Tanihata et al. Recent experimental progress in nuclear halo structure studies. *Progress in Particle and Nuclear Physics*, 68:215–313, 2013.

[25] C. Rodríguez-Tajes et al. Structure of ^{22}N and the $N = 14$ subshell. *Phys. Rev. C*, 83:064313, Jun 2011.

[26] M. J. Strongman et al. Disappearance of the $N = 14$ shell. *Phys. Rev. C*, 80:021302, Aug 2009.

[27] Z. Elekes et al. Nuclear structure study of ^{19,21}N nuclei by γ spectroscopy. *Phys. Rev. C*, 82:027305, Aug 2010.

[28] M. Belleguic et al. In-beam γ-spectroscopy using projectile fragmentation: Structure of neutron-rich nuclei around N=20. *Nuclear Physics A*, 682(1):136–142, 2001.

[29] A. Schiller et al. Selective Population and Neutron Decay of an Excited State of ^{23}O. *Phys. Rev. Lett.*, 99:112501, Sep 2007.

[30] E. Becheva et al. $n = 14$ shell closure in ^{22}O viewed through a neutron sensitive probe. *Phys. Rev. Lett.*, 96:012501, Jan 2006.

[31] E. Becheva et al. $n = 14$ shell closure in ^{22}O viewed through a neutron sensitive probe. *Phys. Rev. Lett.*, 96:012501, Jan 2006.

[32] P. Díaz Fernández et al. Quasifree (p, pN) scattering of light neutron-rich nuclei near N=14. *Phys. Rev. C*, 97:024311, Feb 2018.

[33] D Sohler et al. In-beam gamma-ray spectroscopy of the neutron-rich nitrogen isotopes $^{19-22}$N. *Physical Review C*, 77(4), 2008.

[34] S. Bagchi et al. Neutron skin and signature of the N = 14 shell gap found from measured proton radii of $^{17-22}$N. *Physics Letters B*, 790:251–256, 2019.

[35] A. Ozawa et al. Measurements of interaction cross sections for light neutron-rich nuclei at relativistic energies and determination of effective matter radii. *Nuclear Physics A*, 691(3):599–617, 2001.

[36] M. Wang et al. The AME2012 atomic mass evaluation. *Chinese Physics C*, 36(12):1603, dec 2012.

[37] M. Wang et al. The AME2016 atomic mass evaluation (II). Tables, graphs and references. *Chinese Physics C*, 41(3):030003, mar 2017.

[38] I. Angeli et al. Table of experimental nuclear ground state charge radii: An update. *Atomic Data and Nuclear Data Tables*, 99(1):69–95, 2013.

[39] Y. Togano et al. Interaction cross section study of the two-neutron halo nucleus ^{22}C. *Physics Letters B*, 761:412–418, October 2016.

[40] R. Hofstadter. Electron scattering and nuclear structure. *Rev. Mod. Phys.*, 28:214–254, Jul 1956.

[41] F. P. Juster et al. Tritium Electromagnetic Form Factors. *Phys. Rev. Lett.*, 55:2261–2264, Nov 1985.

[42] F.J. Kline et al. Elastic electron scatterring from ^{14}C. *Nuclear Physics A*, 209(2):381–395, 1973.

[43] T. Ohnishi et al. The SCRIT electron scattering facility project at RIKEN RI beam factory. *Physica Scripta*, 2015(T166):014071, nov 2015.

[44] G. Fricke et al. Nuclear Ground State Charge Radii from Electromagnetic Interactions. *Atomic Data and Nuclear Data Tables*, 60(2):177–285, 1995.

[45] A. Adamczak et al. Nuclear structure with radioactive muonic atoms. *EPJ Web Conf.*, 193:04014, 2018.

[46] R. Sánchez et al. Nuclear Charge Radii of ^{9,11}Li: The Influence of Halo Neutrons. *Phys. Rev. Lett.*, 96:033002, Jan 2006.

[47] G. Ewald et al. Nuclear Charge Radii of ^{8,9}Li Determined by Laser Spectroscopy. *Phys. Rev. Lett.*, 93:113002, Sep 2004.

[48] L. B. Wang et al. Laser Spectroscopic Determination of the ^{6}He Nuclear Charge Radius. *Phys. Rev. Lett.*, 93:142501, Sep 2004.

[49] P. Mueller et al. Nuclear Charge Radius of ^{8}He. *Phys. Rev. Lett.*, 99:252501, Dec 2007.

[50] W. Nörtershäuser et al. Nuclear Charge Radii of ^{7,9,10}Be and the One-Neutron Halo Nucleus ^{11}Be. *Phys. Rev. Lett.*, 102:062503, Feb 2009.

[51] R. F. Garcia Ruiz et al. Unexpectedly large charge radii of neutron-rich calcium isotopes. *Nature Physics*, 12(6):594–598, Jun 2016.

[52] W. R. Webber et al. Individual charge changing fragmentation cross sections of relativistic nuclei in hydrogen, helium, and carbon targets. *Phys. Rev. C*, 41:533–546, Feb 1990.

[53] J. R. Cummings et al. Determination of the cross sections for the production of fragments from relativistic nucleus-nucleus interactions. I. Measurements. *Phys. Rev. C*, 42:2508–2529, Dec 1990.

[54] B. Blank et al. Charge-changing cross sections of the neutron-rich isotopes ^{8,9,11}Li. *Zeitschrift für Physik A Hadrons and Nuclei*, 343(4):375–379, Dec 1992.

[55] L.V. Chulkov et al. Total charge-changing cross sections for neutron-rich light nuclei. *Nuclear Physics A*, 674(3):330–342, 2000.

[56] M. E. Rose. Theoretical Physics. *Science*, 143(3605):460–460, 1964.

[57] Paul J. Karol. Nucleus-nucleus reaction cross sections at high energies: Soft-spheres model. *Phys. Rev. C*, 11:1203–1209, Apr 1975.

[58] Y. Suzuki et al. Parameter-free calculation of charge-changing cross sections at high energy. *Phys. Rev. C*, 94:011602, Jul 2016.

[59] B. Abu-Ibrahim et al. Reaction cross sections of carbon isotopes incident on a proton. *Phys. Rev. C*, 77:034607, Mar 2008.

[60] A. Estradé et al. Proton Radii of $^{12-17}$B Define a Thick Neutron Surface in ^{17}B. *Phys. Rev. Lett.*, 113:132501, Sep 2014.

[61] R. Kanungo et al. Proton Distribution Radii of $^{12-19}$C Illuminate Features of Neutron Halos. *Phys. Rev. Lett.*, 117:102501, Sep 2016.

[62] T. Yamaguchi et al. Scaling of Charge-Changing Interaction Cross Sections and Point-Proton Radii of Neutron-Rich Carbon Isotopes. *Phys. Rev. Lett.*, 107:032502, Jul 2011.

[63] Yano Y. The RIKEN RI Beam Factory Project: A status report. *Nuclear Instruments and Methods in Physics Research Section B: Beam Interactions with Materials and Atoms*, 261(1):1009–1013, 2007. The Application of Accelerators in Research and Industry.

[64] T. Kubo et al. BigRIPS separator and ZeroDegree spectrometer at RIKEN RI Beam Factory. *Progress of Theoretical and Experimental Physics*, 2012(1):03C003, 12 2012.

[65] https://www.riken.jp/en/collab/resources/ribf/.

[66] M. Tanaka. *Determination of nuclear matter radii of Ca isotopes across the neutron magic number N = 28 via interaction cross-section measurements*. PhD thesis, 2018.

[67] A. Ozawa. Nuclear size and related topics. *Nuclear Physics A*, 693(1):32–62, 2001. Radioactive Nuclear Beams.

[68] S. Bagchi et al. Two-Neutron Halo is Unveiled in ^{29}F. *Phys. Rev. Lett.*, 124:222504, Jun 2020.

[69] K. Kimura et al. High-rate particle identification of high-energy heavy ions using a tilted electrode gas ionization chamber. *Nuclear Instruments and Methods in Physics Research Section A: Accelerators, Spectrometers, Detectors and Associated Equipment*, 538(1):608–614, 2005.

[70] Steven P. Ahlen. Theoretical and experimental aspects of the energy loss of relativistic heavily ionizing particles. *Rev. Mod. Phys.*, 52:121–173, Jan 1980.

[71] H. Kumagai et al. Development of Parallel Plate Avalanche Counter (PPAC) for BigRIPS fragment separator. *Nuclear Instruments and Methods in Physics Research Section B: Beam Interactions with Materials and Atoms*, 317:717–727, 2013. XVIth International Conference on ElectroMagnetic Isotope Separators and Techniques Related to their Applications, December 2–7, 2012 at Matsue, Japan.

[72] K. Wang et al. Plastic scintillation detectors for time-of-flight mass measurements. *Nuclear Instruments and Methods in Physics Research Section A: Accelerators, Spectrometers, Detectors and Associated Equipment*, 974:164199, 2020.

[73] T. Baumann. *Longitudinal Momentum Distributions of ^{8}B and ^{19}C : Signatures for One-Proton and One-Neutron Halos*. PhD thesis, Darmstadt University, 1999.

[74] S. Das. A simple alternative to the Crystal Ball function, 2016.

[75] http://lise.nscl.msu.edu/.